The Development and Characterization of Ion Detectors and Levitated Ion Sources for Time-of-Flight Mass Spectrometry

By

Ranran Liu

A dissertation submitted in partial fulfillment of the requirements for the degree of

Doctor of Philosophy

(Chemistry)

at the

UNIVERSITY OF WISCONSIN-MADISON

2015

Date of final oral examination: 1/22/15

The dissertation is approved by the following members of the Final Oral Committee:

Lloyd M. Smith, Professor, Chemistry
John C. Wright, Professor, Chemistry
Lingjun Li, Professor, Pharmacy
Etienne Garand, Professor, Chemistry
Timothy H. Bertram, Professor, Chemistry

TABLE OF CONTENTS

ACKNOWLEDGEMENTS

First and foremost, I would like to thank my advisor, Professor Lloyd M. Smith, for his patience, guidance, support and trust. I learned a lot from him in knowledge, perspective and scientific thinking. The freedom he provides to his students is such a privilege to have in a research laboratory.

I would like to give my special thanks to Professor Frank N. Keutsch and Professor Robert H. Blick for their valuable advice and support in the collaborative projects. I appreciate very much the kindness of all Smith group members, past and present, and their helpful suggestions. I whish to acknowledge the help provided by everybody I worked with in the past four and a half years, especially Dr. Brian Frey, Dr. Hyunseok Kim, Ge Yu, Qiyao Li and Sean Staudt. I would like to thank Dr. Michael Westphall, Dr. Ryan Hilger and Dr. Rob McClain for helpful discussions, and Christina Lampe, Jana von Poblotzki and Dr. Diana Hildebrand for the constant supply of nanomembranes. Continuous assistance provided by the technicians in the machine shop and electronic shop and many friends in other research groups in the Chemistry Department is greatly appreciated. I feel so blessed to have the chance to know them all.

Finally, I would like to express my sincere gratitude to my family, especially my mother and father, for their encouragement and love throughout my life. I would also like to thank my fiancé Di Zhu, who has always been supporting me and making my life more wonderful than I can ever imagine for the last nine years.

PREFACE

The work presented in this dissertation was performed at the University of Wisconsin-Madison under the supervision of Professor Lloyd M. Smith. It describes research on the development and characterization of ion detectors and levitated ion sources for mass spectrometry (MS).

The dissertation is separated into two sections. Section 1 includes Chapters 1 to 3, which presents the work in the characterization of ion detectors in Time-of-Flight (TOF) mass spectrometry. Section 2 includes Chapter 4, which presents the work in the development of a new ion source for the mass spectrometric analysis of a levitated droplet. Chapter 1 gives a brief introduction to TOF-mass spectrometry and TOF-MS detectors. Chapter 2 presents a detailed characterization of the response of the most widely used TOF-MS detector, the microchannel plate, as a function of ion mass and acceleration voltage. This work, except for section 2.3.5, was published in *Journal of the American Society for Mass Spectrometry*, volume 25, pages 1374-1383, 2014 under the title "Detection of Large Ions in Time-of-Flight Mass Spectrometry: Effects of Ion Mass and Acceleration Voltage on Microchannel Plate Detector Response." Ranran Liu designed and performed experiments, analyzed the data and wrote the paper. Qiyao Li performed experiments. Lloyd M. Smith designed experiments and wrote the paper. Chapter 3 presents the study of a novel nanomembrane detector for TOF-MS with varying nanomembrane composition, ion mass and ion energy. This work is a collaborative project with Professor Robert H. Blick and his colleagues at the University of Hamburg

in Germany (previously in the UW-Madison). Chapter 4 describes a new instrument that combines optical trapping with MS for the study of multi-phase chemistry in a single aerosol droplet. This work is a collaborative project with Professor Frank N. Keutsch at Harvard University (previously in the UW-Madison) and his colleagues. The work presented in Chapters 3 and 4 have not been published.

The Development and Characterization of Ion Detectors and Levitated Ion Sources for Time-of-Flight Mass Spectrometry

Ranran Liu

Under the supervision of Professor Lloyd M. Smith

at the University of Wisconsin-Madison

ABSTRACT

Mass spectrometry (MS) plays an important role in the analysis of complex protein samples, which is performed primarily with two strategies: the bottom-up and top-down approaches. The latter has the advantage of preserving the crucial protein-level information by directly analyzing the intact proteins. Time-of-flight (TOF) mass spectrometry is heavily employed in intact protein detection due to its compatibility with the high m/z range of singly charged proteins produced by matrix-assisted laser desorption/ionization (MALDI). However, a significant challenge in TOF-MS is the limited efficiency of detecting large and slow-moving protein ions. Part of the reason lies in the TOF detectors. Conventional detectors, i.e. electron multipliers and microchannel plate (MCP) detectors, are based upon the generation of secondary electrons at ion collision, which is well known to have a decreasing efficiency as the ion velocity decreases. This relationship between ion mass and ion detection efficiency is characterized in detail. The response of an MCP detector as a function of ion mass and acceleration voltage was

characterized, for singly charged peptide/protein ions ranging from 1 to 290 kDa in mass, and for acceleration voltages from 5 to 25 kV.

New types of detectors are under development to overcome the detection limit for large molecules. We are developing a novel nanomembrane detector, which contains a freestanding nanomembrane that responds to ion collisions with field emission current changes. The detection efficiencies and mechanisms of different nanomembranes for 9 peptide/protein samples at various acceleration voltages were explored in a MALDI-TOF instrument.

Atmospheric aerosols have serious influences on our climate and health. Understanding of their formation is important but difficult with current research tools. We are developing a novel experimental approach that combines optical tweezers for droplet levitation with control of gas-phase composition and droplet analysis using TOF mass spectrometry. MS analysis of a levitated droplet in a Bessel beam optical tweezers was performed using electrospray ionization and mass spectra of the analyte in the droplet were obtained.

Section 1

CHAPTER 1

Introduction

The critical protein actors in biological systems are the intact proteoforms, namely the different forms of proteins, produced from the genome in a variety of splice forms, and adorned with a myriad of post-translational modifications that modulate their function[1]. A challenging problem in proteomics, the large-scale study of proteins, particularly their structures and functions, is the development of new approaches to the analysis of complex proteoform mixtures, revealing the identities and abundances of all detectable proteoforms present[2, 3]. Mass spectrometry (MS) has become the method of choice for analysis of complex protein samples due to its high sensitivity and versatility.

A mass spectrometer is a system that measures the amount and mass-to-charge ratio (m/z) of gas-phase ions. It consists of three main parts: an ionization source that converts molecules to ions, a mass analyzer that separates ions by their m/z, and an ion detector that quantifies the ions[4]. MS started to play an important role in proteomics since the 1980s, after the discovery of protein ionization methods. Before that, transferring the biomolecules into the gas phase and then ionizing them was not easily accomplished[5]. Currently, there are two complementary lines of attack for the mass spectrometric analysis of proteins: the bottom-up and top-down approaches[6]. The

bottom-up approach, in which proteins are degraded into peptides before MS analysis, is widely used for determining the details of protein sequence and posttranslational modifications[7]. However, the crucial protein-level information is lost during protein digestion. This is avoided in the top-down approach, which directly generates intact protein ions that are subsequently fragmented in the mass spectrometer. The molecular masses of both the intact protein and the fragment ions are measured[8].

The two widely used protein ionization methods are electrospray ionization (ESI)[9] and matrix-assisted laser desorption/ionization (MALDI)[10, 11]. A protein ion generated by ESI usually carries multiple charges, resulting in a high charge per unit mass. This brings two major issues to the MS analysis of proteins: complicated mass spectra and lower signal intensities. Much effort has been put into charge reduction of ESI-generated ions to address these problems[12-14]. In contrast with ESI, MALDI has the advantage of producing predominantly singly charged ions.

The singly charged protein ions must be analyzed by time-of-flight mass spectrometry (TOF-MS), as this is the only mass analyzer able to accommodate the high m/z range of such singly charged proteins. MALDI-TOF mass spectrometers are heavily employed in tissue imaging for biomarker discovery owing to their compatibility with special sample preparation techniques[15]. However, MALDI yields broad peaks and low sensitivity for proteins above about 30 kDa[5], and thus is usually used to detect moderately abundant proteins <50 kDa[16]. This limitation is determined in part by deficiencies of existing MS instrumentation[17, 18]. One of the significant

instrumentation challenges to consider is the efficiency of detecting the large, slow-moving protein ions produced in TOF-MS.

There are three primary mechanisms for the detection of ions in mass spectrometry; these are direct charge detection (as in the Faraday cup detector), image charge detection (as in the inductive detector), and secondary electron generation (as in electron multiplier (EM) and microchannel plate (MCP) detectors)[19]. Direct charge detection is important historically, but finds use almost solely in magnetic sector instruments because of its relatively low sensitivity compared to other detector types. Inductive detectors, although even less sensitive than direct charge detectors, are the only non-destructive detection modality, and hence are critical to Fourier transform instruments such as the Fourier transform ion cyclotron resonance (FTICR) and Orbitrap mass analyzers, where signal averaging of circulating ion packets is fundamental to the instrument's operation. TOF ion detectors need to have large areas, rapid response times to provide good timing resolution and correspondingly accurate m/z determinations, and high sensitivity. These criteria are best met by the EM and MCP detectors, based upon their generation of secondary electrons[4].

Secondary electrons are emitted from surfaces upon ion collision. The emission involves multiple processes and complex mechanisms[20]. In EM and MCP detectors, secondary electrons generated by the impinging protein ions are accelerated down the channel by a positive bias. The electrons strike the channel walls to produce additional electrons and are eventually amplified to a detectable level[21]. Studies have revealed the

secondary electron emission yield, i.e. the average yield of secondary electrons per incident ion, is related to ion mass, velocity and atomic shell structure[22]. It is well established that the secondary electron yield decreases as velocity of the molecular ion decreases[23-26]. The direct result of this decreased yield is the limited ion detection efficiency for large protein ions that travel much slower than small ions in TOF-MS. The signal of large ions may appear artificially low or possibly not be detected at all. Measurements have been made to characterize the secondary electron yield of large molecular ions on various surfaces[21, 22, 27] and on MCP detectors as well[20, 28, 29]. Empirical functions of secondary electron yield have been determined for ions in the kilodalton mass range, which is typical for TOF-MS studies. In general, the MCP detector response increases proportionally to ion mass, but decreases with a roughly fourth-order dependence on ion velocity[29]. Chapter 2 presents a detailed characterization of MCP response as a function of ion mass and acceleration voltage in a velocity range of 3.5 to 68 km/s.

With the conventional MCP detectors, detection of ions larger than 1 MDa is very challenging[30]. New types of detectors have been developed to overcome the detection limit for large molecules. One main type of high-mass detectors is based on secondary ion emission, which is more efficient for high mass ions than is secondary electron emission. The detectors use conversion dynodes to create smaller secondary ions from incident primary ions, which are then reaccelerated into an electron multiplier for amplification[31]. These detectors allow detection of ions up to the megadalton range

and have been successfully applied to the studies of protein-protein interactions[32, 33]. Another alternative to MCP detectors are cryogenic detectors[34-36]. They measure low-energy solid-state excitations, known as phonons, created by a particle impact in the form of heat[37]. The cryogenic detectors are sensitive enough for single ion detection and are able to detect all ions with equal efficiency in a MALDI-TOF mass spectrometer. However, cryogenic detectors are very small (0.05-0.2 mm in one dimension) and require an operating temperature below 1 K[38]. Recently, a highly sensitive active pixel detector that was originally designed for high-energy electron and photon detection has been employed in TOF-MS[39]. It consists of 262,144 parallel detectors where each pixel is a Si detector coupled to a complementary metal oxide semiconductor (CMOS) pixel read-out chip[40, 41]. By placing it behind a MCP, the electrons produced by an ion packet can be detected and the mass spectra show a significant enhancement in signal-to-noise ratios for molecules as large as immunoglobulin G (147 kDa) and immunoglobulin A (400 kDa)[39].

We developed a novel detector that utilizes a freestanding nanomembrane to sense ion impact[42]. The kinetic energy of impinging ions transferred to the nanomembrane upon collision ultimately induces variations in electrons emitted from the nanomembrane under a strong electrical field. Since ion kinetic energy is determined by ion charge and acceleration voltage in MALDI-TOF analysis, the nanomembrane detector response should be independent of ion mass. Chapter 3 summarizes the effects

of nanomembrane composition, ion mass and ion energy on the performance of the nanomembrane detector in a MALDI-TOF instrument.

In addition to the work on the characterization and development of TOF-MS detectors presented in Chapters 2 and 3, I have been working on the development of a new approach for the online and *in situ* characterization of a single aerosol droplet accomplished with combining droplet levitation techniques and mass spectrometry, which is described in Chapter 4.

REFERENCES

1. Smith, L.M., Kelleher, N. L., The Consortium for Top Down Proteomics. Proteoform: a single term describing protein complexity. *Nat. Methods*. **10**(3), 186-187 (2013).

2. Kellie, J.F., Catherman, A.D., Durbin, K.R., Tran, J.C., Tipton, J.D., Norris, J.L., Witkowski, C.E., II, Thomas, P.M., Kelleher, N.L. Robust analysis of the yeast proteome under 50 kDa by molecular-mass-based fractionation and top-down mass spectrometry. *Anal. Chem.* **84**(1), 209-215 (2012).

3. Tran, J.C., Zamdborg, L., Ahlf, D.R., Lee, J.E., Catherman, A.D., Durbin, K.R., Tipton, J.D., Vellaichamy, A., Kellie, J.F., Li, M., Wu, C., Sweet, S.M., Early, B.P., Siuti, N., LeDuc, R.D., Compton, P.D., Thomas, P.M., Kelleher, N.L. Mapping intact protein isoforms in discovery mode using top-down proteomics. *Nature*. **480**(7376), 254-258 (2011).

4. de Hoffmann, E., Stroobant, V. Mass Spectrometry Principles and Applications, 3rd ed. John Wiley & Sons: Chicester, U.K. (2007).

5. Mann, M., Hendrickson, R.C., Pandey, A. Analysis of Proteins and Proteomes by Mass Spectrometry. *Annu. Rev. Biochem.* **70**, 437-473 (2001).

6. Chait, B.T. Mass spectrometry: bottom-up or top-down? *Science*. **314**(5796), 65-66 (2006).

7. Aebersold, R., Mann, M. Mass spectrometry-based proteomics. *Nature*. **422**(6928), 198-207 (2003).

8. Wysocki, V.H., Resing, K.A., Zhang, Q., Cheng, G. Mass spectrometry of peptides and proteins. *Methods*. **35**(3), 211-222 (2005).

9. Fenn, J.B., Mann, Matthias, Meng, C.K., Wong, S.F., Whitehouse, C.M. Electrospray Ionization for Mass Spectrometry of Large Biomolecules. *Science*. **246**(4926), 64-71 (1989).

10. Tanaka, K., Waki, H., Ido, Y., Akita, S., Yoshida, Y., Yoshida, T., Matsuo, T. Protein and polymer analyses up to m/z 100 000 by laser ionization time-of-flight mass spectrometry. *Rapid Commun. Mass Spectrom.* **2**(8), 151-153 (1988).

11. Hillenkamp, F., Karas, M., Beavis, R.C., Chait, B.T. Matrix-assisted laser desorption/ionization mass spectrometry of biopolymers. *Anal. Chem.* **63**(24), 1193A-1203A (1991).

12. Scalf, M., Westphall, M.S., Smith, L.M. Charge Reduction Electrospray Mass Spectrometry. *Anal. Chem.* **72**(1), 52-60 (1999).

13. Stephenson, J.L., McLuckey, S.A. Ion/Ion Reactions in the Gas Phase: Proton Transfer Reactions Involving Multiply-Charged Proteins. *J. Am. Chem. Soc.* **118**(31), 7390-7397 (1996).

14. Lee, J., Chen, H., Liu, T., Berkman, C.E., Reilly, P.T. High resolution time-of-flight mass analysis of the entire range of intact singly-charged proteins. *Anal. Chem.* **83**(24), 9406-9412 (2011).

15. Caprioli, R.M., Farmer, T.B., Gile, J. Molecular Imaging of Biological Samples: Localization of Peptides and Proteins Using MALDI-TOF MS. *Anal. Chem.* **69**(23), 4751-4760 (1997).

16. Kelleher, N.L. Top-down proteomics. *Anal. Chem.* **76**(11), 197A-203A (2004).

17. Chen, X., Westphall, M.S., Smith, L.M. Mass Spectrometric Analysis of DNA Mixtures: Instrumental Effects Responsible for Decreased Sensitivity with Increasing Mass. *Anal. Chem.* **75**(21), 5944-5952 (2003).

18. Weidmann, S., Mikutis, G., Barylyuk, K., Zenobi, R. Mass discrimination in high-mass MALDI-MS. *J. Am. Soc. Mass Spectrom.* **24**(9), 1396-1404 (2013).

19. Geno, P.W. Ion Detection in Mass Spectrometry, in *Mass Spectrometry in the Biological Sciences: A Tutorial*, pp. 133-142. Springer, Netherlands (1992)

20. Gilmore, I.S., Seah, M.P. Ion detection efficiency in SIMS: dependencies on energy, mass and composition for microchannel plates used in mass spectrometry. *Int. J. Mass Spectrom.* **202**(1-3), 217-229 (2000).

21. Westmacott, G., Ens, W., Standing, K.G. Secondary ion and electron yield measurements for surfaces bombarded with large molecular ions. *Nucl. Instrum. Meth. B*. **108**(3), 282-289 (1996).

22. Beuhler, R.J., Friedman, L. Threshold studies of secondary electron emission induced by macro-ion impact on solid surfaces. *Nucl. Instrum. Meth.* **170**(1-3), 309-315 (1980).

23. Axelsson, J., Reimann, C.T., Sundqvist, B.U.R. Secondary electron emission from surfaces impacted by multiply-charged polyatomic ions. *Nucl. Instrum. Meth. B*. **88**(1-3), 131-137 (1994).

24. Axelsson, J., Parilis, E.S., Reimann, C.T., Sullivan, P., Sundqvist, B.U.R. Electron emission from conducting surfaces impacted by multiply-charged polyatomic ions. *Nucl. Instrum. Meth. B*. **101**(4), 343-356 (1995).

25. Axelsson, J., Reimann, C.T., Sundqvist, B.U.R. Secondary electron resolved mass spectrometry of electrosprayed ions. *Int. J. Mass Spectrom.* **133**(2-3), 141-155 (1994).

26. Beuhler, R.J. A comparison of secondary electron yields from accelerated water cluster ions (M/z<50 000) striking Al_2O_3 and copper surfaces. *J. Appl. Phys.* **54**(7), 4118-4126 (1983).

27. Brunelle, A., Chaurand, P., Della-Negra, S., Le Beyec, Y., Parilis, E. Secondary Electron Emission Yields from a CsI Surface Under Impacts of Large Molecules at Low Velocities (5×10^3–7×10^4 ms^{-1}). *Rapid Commun. Mass Spectrom.* **11**(4), 353-362 (1998).

28. Geno, P.W., Macfarlane, R.D. Secondary electron emission induced by impact of low-velocity molecular ions on a microchannel plate. *Int. J. Mass Spectrom.* **92**, 195-210 (1989).

29. Westmacott, G., Frank, M., Labov, S.E., Benner, W.H. Using a superconducting tunnel junction detector to measure the secondary electron emission efficiency for a microchannel plate detector bombarded by large molecular ions. *Rapid Commun. Mass Spectrom.* **14**(19), 1854-1861 (2000).

30. Lin, H.C., Lin, J.L., Chen, C.H. Novel mass spectrometry technology development for large organic particle analysis. *RSC Adv.* **4**(9), 4523-4534 (2014).

31. van Remoortere, A., van Zeijl, R.J., van den Oever, N., Franck, J., Longuespee, R., Wisztorski, M., Salzet, M., Deelder, A.M., Fournier, I., McDonnell, L.A. MALDI imaging and profiling MS of higher mass proteins from tissue. *J. Am. Soc. Mass Spectrom.* **21**(11), 1922-1929 (2010).

32. Bich, C., Scott, M., Panagiotidis, A., Wenzel, R. J., Nazabal, A., Zenobi, R. Characterization of antibody-antigen interactions: comparison between surface plasmon resonance measurements and high-mass matrix-assisted laser desorption/ionization mass spectrometry. *Anal. Biochem.* **375**(1), 35-45 (2008).

33. Pimenova, T., Pereira, C.P., Schaer, D.J., Zenobi, R. Characterization of high molecular weight multimeric states of human haptoglobin and hemoglobin-based oxygen carriers by high-mass MALDI MS. *J. Sep. Sci.* **32**(8), 1224-1230 (2009).

34. Wenzel, R.J., Matter, U., Schultheis, L., Zenobi, R. Analysis of megadalton ions using cryodetection MALDI Time-of-Flight mass spectrometry. *Anal. Chem.* **77**(14), 4329-4337 (2005).

35. Hilton, G.C., Martinis, J.M., Wollman, D.A., Irwin, K.D., Dulcie, L.L., Gerber, D., Gillevet, P.M., Twerenbold, D. Impact energy measurement in Time-of-Flight mass spectrometry with cryogenic microcalorimeters. *Nature*. **391**(6668), 672-675 (1998).

36. Frank, M. Mass spectrometry with cryogenic detectors. *Nucl. Instrum. Meth. A*. **444**(1-2), 375-384 (2000).

37. Peng, W.P., Chou, S.W., Patil, A.A. Measuring masses of large biomolecules and bioparticles using mass spectrometric techniques. *Analyst*. **139**(14), 3507-3523 (2014).

38. Frank, M., Labov, S.E., Westmacott, G., Benner, W.H. Energy-sensitive cryogenic detectors for high-mass biomolecule mass spectrometry. *Mass Spectrom. Rev.* **18**(3-4), 155-186 (1999).

39. Ellis, S.R., Jungmann, J.H., Smith, D.F., Soltwisch, J., Heeren, R.M. Enhanced detection of high-mass proteins by using an active pixel detector. *Angew. Chem. Int. Ed.* **52**(43), 11261-11264 (2013).

40. Kiss, A., Jungmann, J.H., Smith, D.F., Heeren, R.M. Microscope mode secondary ion mass spectrometry imaging with a Timepix detector. *Rev. Sci. Instrum.* **84**(1), 013704 (2013).

41. Jungmann, J.H., MacAleese, L., Buijs, R., Giskes, F., de Snaijer, A., Visser, J., Visschers, J., Vrakking, M.J., Heeren, R.M. Fast, high resolution mass spectrometry imaging using a Medipix pixelated detector. *J. Am. Soc. Mass Spectrom.* **21**(12), 2023-2030 (2010).

42. Park, J., Qin, H., Scalf, M., Hilger, R.T., Westphall, M.S., Smith, L.M., Blick, R.H. A mechanical nanomembrane detector for Time-of-Flight mass spectrometry. *Nano Lett.* **11**(9), 3681-3684 (2011).

CHAPTER 2

Detection of Large Ions in Time-of-Flight Mass Spectrometry: Effects of Ion Mass and Acceleration Voltage on Microchannel Plate Detector Response

2.1 INTRODUCTION

Detection of singly charged protein ions in Time-of-Flight mass spectrometry (TOF-MS) is well known to be inefficient and challenging. One of the main reasons is the reduced efficiency of conventional TOF detectors, i.e. electron multipliers (EM) and microchannel plate (MCP) detectors, at detection of large ions[1]. A crucial process in ion detection with EMs and MCP detectors is the production of secondary electrons, which highly depends on ion mass and velocity[2]. In TOF mass analyzers, all ions generated in the source are subjected to the same acceleration voltage U, and thus, to first order, all singly charged ions acquire the same kinetic energy, $qU = 1/2mv^2$, where q is the ion charge, m is the ion mass, and v is the ion velocity[3]. Singly charged ions of greater mass therefore necessarily move more slowly than smaller ions, and thus impinge upon the detector with lower velocity. Previous work has characterized MCP response as a function of ion mass and velocity and shown the detector response increases

proportionally to ion mass, but decreases with a roughly fourth-order dependence on ion velocity[4]. However, this work only examined a mass range up to 66 kDa, and accordingly left unaddressed the question of how MCPs respond to protein ions outside that range. In the human proteome, for example, more than a third of proteins have masses over 50 kDa[5], and thus the issue of ion detection sensitivity for these large macromolecular species is critical. It is important to characterize the performance of these existing detectors in order to be able to evaluate their merits relative to potential alternative detection modalities[6-8].

We present here a detailed characterization of MCP response as a function of ion mass and acceleration voltage. We analyzed a set of 10 peptide/protein ions ranging in mass from 1 to 294 kDa, a four-fold greater mass range than previous studies, and subjected them to acceleration voltages from 5 to 25 kilovolts (kV). The values of the secondary electron yield γ (average number of electrons produced per ion collision), and the detection efficiency ε (probability of generation of one or more secondary electrons) were determined for each peptide/protein and acceleration voltage. Ions generated in the MALDI source are detected in parallel by both an in-line non-destructive inductive charge detector (ICD) mounted in the flight tube, and an MCP detector positioned at the end of the flight tube. When ions pass through the conducting cylinder of the ICD, image charges are induced on the cylinder surface and amplified to a detectable signal. The ICD provides an absolute measure of the number of ions present in the ion packet, allowing an accurate calibration of the MCP response. ICDs are primarily employed in

Fourier transform ion cyclotron resonance (FTICR) instruments and electrodynamic ion traps. The signal-to-noise ratio of ICD is intrinsically low but can be greatly improved by signal averaging as ions cycling back and forth through the same detector[9]. Fuerstenau and Benner performed the detection of megadalton DNA ions using an inductive charge detector installed in a TOF mass spectrometer[10]. Their work inspired a number of other applications of the inductive detector[11-14] in TOF-MS and also the development of new charge detectors with a detection limit as low as 9 charges[9, 15].

2.2 EXPERIMENTAL

2.2.1 Reagents and Materials

All peptides, proteins, matrices and solvents were obtained from Sigma-Aldrich (St. Louis, MO). The peptide/protein standards are listed in Table 2.1. Angiotensin II, adrenocorticotropic hormone (ACTH) fragment 18-39, insulin, cytochrome c, apomyoglobin, aldolase, and albumin were purchased as ProteoMass™ MALDI-MS standards and dissolved in 0.1% trifluoroacetic acid (TFA) to 100 μM, except for insulin in 1% TFA. Phosphorylase b (rabbit muscle) and IgG (rabbit serum) were dissolved in 50% acetonitrile/50% (0.05% TFA) to 100 μM. α-Cyano-4-hydroxycinnamic acid (CHCA) and sinapinic acid were prepared as nearly saturated solutions at 10 mg/mL in 50% acetonitrile/50% (0.05% TFA). CHCA was used as matrix for angiotensin II, ACTH fragment, insulin and cytochrome c, while sinapinic acid was employed for the other proteins. MALDI samples were prepared by combining 0.7 μL of matrix solution

with 0.7 μL of sample solution directly on the stainless steel MALDI sample plate, followed by solvent evaporation at atmospheric pressure and room temperature.

2.2.2 Instrumentation

Experiments were performed on a modified linear Voyager-DE STR mass spectrometer (Perseptive Biosystems, Framingham, MA) diagrammed in Figure 2.1a. The ions were detected at the end of the flight tube with the manufacturer-supplied High Current Detector (HCD). This detector consists of a nichrome-coated MCP followed by a scintillator that converts electrons to photons, which are then detected with a photosensor module (Type No. H5773, Hamamatsu Photonics, Bridgewater, NJ). This single MCP detector is less susceptible to saturation than the dual chevron MCP employed in a previous study[1]. The MCP has the following properties; 40 mm quality diameter, 32 μm channel center-to-center spacing, 25 μm channel diameter, 8° bias angle, 40:1 aspect ratio, 30-125 μA bias current, and was obtained from JBI Scientific (Huntsville, TX) to replace the original MCP. The MCP was operated at a potential of 960 V for all experiments reported here. The photosensor module is controlled by an attached circuit board that also provides a suitable output voltage (referred to below as the "MCP voltage"), which was monitored in the present work with a Tektronix DPO 2024B oscilloscope (Tektronix, Beaverton, OR).

An inductive charge detector (ICD) was placed in the ion path in front of the MCP detector to provide an absolute reference signal for the number of ions present in

each ion packet. The ICD (illustrated in Figure 2.1b was constructed based on the design of Fuerstenau and Benner[10]. As shown in the diagram, it consists of three concentric tubes: The innermost tube is copper, 1.18" in length, with a 0.25" outer diameter and 0.20" inner diameter, and serves as the image charge sensing element. It is positioned in contact with a piece of 22 gauge stranded silver coated copper wire in the center of the second tube, which is made of Teflon, 2.00" in length, with a 1.51" outer diameter and 0.25" inner diameter, and serves as an insulating spacer. The third outer tube is copper, also 2.00" in length, with a 1.62" outer diameter and 1.51" inner diameter, and serves as a radiofrequency (RF) shield for the image charge pickup tube. The front end of the Teflon tube is mounted on a home-made 4.74" diameter copper disk with a center hole of 0.25" diameter, which also served as the vacuum flange gasket used to join two segments of the flight tube. An 88% transmission electroformed nickel grid (Industrial Netting, Minneapolis, MN) was inserted between the flange and the Teflon tube to provide an RF shield (keeping electric fields due to approaching ions from inducing charge on the detector). This design positions the ICD coaxial with the flight tube while providing important RF shielding protecting the image charge sensor from external fields. The distance between the exit of the ICD and the MCP front surface is 5.0". With this short distance and the large quality diameter of the MCP, all ions passing through the ICD strike the MCP.

Ions passing through the inner tube induce image charges on the tube surface. The tube is connected by the 22-gauge wire to a 2SK152 field-effect transistor (FET)

coupled to an A250 charge-sensitive preamplifier (Amptek, Bedford, MA) for signal processing (see Figure 2.1a). The electronic components are installed on an in-house fabricated circuit board, which is enclosed in an aluminum box placed inside of the flight tube to minimize RF pickup. The feedback loop of the preamplifier contains a 1 GΩ resistor and a parasitic capacitance C_f estimated to be about 0.13 picofarad (pF). This estimate is obtained by using the circuit to measure a known quantity of charge placed on a 2.2 pF test capacitor (C_{test}) with an 80 mV input voltage (V_{in}). The output voltage peak value is given by $V_{out} = V_{in}C_{test}/C_f$. This equation also shows that maximum gain is obtained when the feedback capacitance is minimized. A similar measurement applying V_{in} to the outer copper tube instead of a test capacitor yields a capacitance between the two copper tubes of 3.4 pF. The large feedback resistor is required to keep the RC time constant (in this case, 130 μs) much longer than the time required for the slowest ion packet to pass entirely through the ICD. This prevents the output signal from starting to decrease before it reaches the peak value. The output of the preamplifier is connected to the oscilloscope with the input impedance set to 1 MΩ.

2.2.3 MALDI-TOF analysis

Mass spectra were acquired in positive ion mode at five acceleration voltages (5kV, 10kV, 15kV, 20kV, 25 kV), with acquisition parameters (grid voltage, delayed extraction time and guide wire voltage) optimized for each analyte. At least 3 spectra were taken at six to eight different laser intensities in order to vary the ion yield. Each spectrum was an

average of signals from 50 laser shots. Spectra obtained from the ICD and MCP were acquired simultaneously on different channels of an oscilloscope, and were thereby automatically synchronized in data acquisition, for both channels were triggered by the same signal provided by the laser upon firing.

2.2.4 MCP detector efficiency measurements

Overview. The ICD is employed here to provide an absolute measure of the number of ions present in each ion packet, allowing an accurate calibration of the MCP response. The manner in which this is accomplished is described below.

ICD signal. When an ion packet with N_i ions carrying a charge Q is present in the ICD, an opposite charge less than or equal to Q is induced on the ICD and converted to a voltage by the charge-sensitive preamplifier. For clarity, the induced charge is approximated here as equal to Q. The intensity of the ICD signal I_{ICD} is a voltage proportional to the amount of charge

$$I_{ICD} = V_{ICD} = \frac{Q}{C_f} = \frac{N_i z e}{C_f} \tag{1}$$

where C_f is the feedback capacitance of the preamplifier, z is the number of charges on each ion and e is the charge of an electron[14].

MCP signal. In contrast to the ICD, which responds to the charges within it collectively, MCP detectors respond to the ions individually. Each ion entering one of the microchannels may eject zero to n secondary electrons from the channel wall, and

these electrons then generate more electrons when they are accelerated into the channel wall by the voltage applied to the MCP. If no secondary electron is emitted initially, the ion is not detected. It has been shown previously that the secondary electron multiplicity is described by a Poisson distribution

$$P_n = \frac{\gamma^n e^{-\gamma}}{n!} \tag{2}$$

where P_n is the probability of emitting n secondary electrons per ion impact, and γ is the average number of secondary electrons emitted per ion impact, known as the secondary electron yield[16].

Calibrating the MCP response with the ICD. To use the ICD signal as a calibration for the MCP response, it is necessary to account for several important differences between the signals at the two detectors. First, the MCP is located further down the flight tube than the ICD, and thus the signals are offset in time. Second, the ion packets expand as they travel down the flight tube, and thus have different lengths at the two detectors. Third, the ion packets are substantially longer in space (typically 10-20 cm) than the length of the ICD (3 cm). It is thus essential to compare only the same part of the ion packets for both detectors, namely the center region yielding the maximum signal intensity. Finally, whereas the ICD signal corresponds to the voltage produced by the ions inside the image charge sensor, the MCP detector produces voltage independently from each microchannel that is activated by an ion collision, and thus the MCP signal for an ion packet corresponds to a sum of the voltages produced from each

time point taken across the peak. The following procedure was employed to process the detector signals to yield a correct calibration, based upon these considerations.

1) Obtain peak time and magnitude of the ion packet from the ICD spectrum.

2) Obtain peak time of the ion packet from the corresponding MCP spectrum.

3) Calculate the velocity of the center ions from the MCP peak time and the distance between the MCP and the sample plate.

4) Calculate the time when the center ions are at the middle of the inner copper tube of the ICD based on their velocity (from 3) and the distance between the ICD and the sample plate.

5) Calculate the velocities of the ions at the inlet and outlet of the inner copper tube separately based on the result of 4) and the inner copper tube length.

6) Calculate the interval (Δt) between the arrivals of the inlet and outlet ions (from 5) at the MCP based on the result of 5) and the distance between the MCP and sample plate.

7) Integrate the MCP voltage across the peak over time range Δt. Move the integral across the MCP peak and find the maximum (the portion of the peak containing the maximum area).

8) A correction is also needed to compensate for the fact that the time interval between data points was longer for spectra acquired on larger, slower-moving ions. Intervals between data points were 32 nsec (angiotensin II, ACTH fragment (15 to 25 kV)), 64 nsec (ACTH fragment (5 kV and 10 kV), insulin), 128 nsec (cytochrome c,

apomyoglobin, aldolase (10 to 25 kV)), or 320 nsec (aldolase (5 kV), albumin, phosphorylase b, IgG). The correction factor f_c is calculated as the time interval employed for the sample, divided by 32 nsec, which was the time interval employed for the shortest mass spectra acquired. The correction factors employed thus have values of 1, 2, 4, or 10.

The intensity of the MCP signal for each spectrum is then given by

$$I_{MCP} = \sum V_{MCP} f_c \tag{3}$$

and may also be expressed as:

$$I_{MCP} = N_e G \tag{4}$$

where N_e is the number of total secondary electrons generated by the ion packet on the MCP channel wall, and G is the voltage resulting from one secondary electron. N_e is given by

$$N_e = N_i f \gamma \tag{5}$$

where f is the open area ratio of the MCP (the ratio of the active MCP area to the entire MCP area). Combining equations (1), (4), and (5) yields the following expression for γ, the secondary electron emission yield:

$$\gamma = \frac{N_e}{N_i f} = \frac{I_{MCP}}{I_{ICD}} z \frac{e}{C_f f G} \tag{6}$$

The constant $\frac{e}{C_f f G}$ was calculated from the results reported by Geno *et al*[2] as 1.6×10^{-5}. They determined secondary electron yield of the bradykinin $[M+H]^+$ ion (1060 Da) at 3.0×10^4 m/s to be 0.50, which is very close to that for the angiotensin II $[M+H]^+$

ion (1046.5 Da) at 3.0×10^4 m/s in the present work due to the similarity in their masses and velocities. Thus, all of the factors in equation (6) are either known, or measured, permitting the calculation of γ for each mass spectrum obtained.

The Poisson distribution shown in equation (2) above permits calculation of the probability that an ion collision with the MCP is detected, by producing one or more secondary electrons. Thus

$$\varepsilon = 1 - P_0 = 1 - e^{-\gamma} \tag{7}$$

where ε is the MCP detection efficiency[2].

MCP detector saturation. The MCP detector is normally operated at high gain (~1000 V) for TOF analysis, in order to provide maximum detection sensitivity[17]. In this mode, substantial numbers of electrons are depleted from the channel wall as the secondary electrons produced in the initial ion collision are amplified exponentially along the channel. Due to the low recharge current, which is limited by the high resistance of the MCP material, the charges depleted from the channel wall require time to be fully replenished. If ions strike the MCP before sufficient recharge time has passed, the gain of the channel is lower and the MCP appears "saturated". This period of time, called "dead time", is on the order of milliseconds, which is longer than the flight time of the slowest ions in this study (0.6 ms) but shorter than the intervals between two laser shots (333 ms).

MCP saturation requires special attention when ion quantification involves signals from the MCP detector. Three situations where the MCP signals are at risk of being reduced by saturation are as follows.

1) Peaks following large matrix ion peaks.

2) Peaks following large analyte peaks within the same spectrum; for example, a singly charged dimer ($[2M+H]^+$) signal may be reduced by a previous large monomer peak ($[M+H]^+$).

3) When the ion density in an ion packet is high, two ions have a higher chance of entering the same channel.

Spectra in which saturation effects were present were identified and eliminated during data processing as described in the following section.

Data processing. The acquired spectra were smoothed by locally weighted scatterplot smoothing (LOESS) to improve signal-to-noise[18]. LOESS employs a smoothing parameter α, which is a measure of the number of data points included in the local averaging process. Larger values of α thus correspond to more smoothing, and lower values of α to less smoothing. As the velocity of the ion increases, the ion packet expands less in its flight direction (due to the shorter flight time) and its peaks on both detectors are narrower. It is thus necessary to reduce α in order to maintain optimum smoothing while retaining peak shape. We found empirically that using the relations α_{MCP} = 13 (km/sec)/velocity (km/sec) for MCP spectra and $\alpha_{ICD} = 4\alpha_{MCP}$ = 52 (km/sec)/velocity (km/sec) for ICD spectra yielded good results. The smoothing parameter employed for the ICD spectra was 4 times greater than that employed for the MCP spectra due to the innate differences in time response of the two detectors. MATLAB was used to perform LOESS for each spectrum and to calculate I_{ICD} and I_{MCP}.

It was also necessary to estimate baselines in order to calculate peak heights in I_{ICD} and I_{MCP} calculations. In the case of the ICD, the estimated peak start point and end point were connected to form a local baseline. I_{ICD} was then calculated by subtracting the value of the baseline at the time of the peak maximum from the peak value. For the MCP spectra, the last 60 data points of the spectrum were taken as the baseline, and I_{MCP} was calculated by subtracting the average value of the baseline from each data point. The (I_{ICD}, I_{MCP}) data set was eliminated if I_{ICD} was below 0.2 mV, as these ICD peaks were too weak to be quantified accurately.

The data sets impacted adversely by MCP saturation were identified by comparing the I_{ICD}/I_{MCP} ratios obtained for a given analyte at the same acceleration voltage. Saturation is more of a problem when higher laser pulse intensities are employed, as this produces higher levels of both matrix and analyte ions. We purposely used a range of laser intensities from near threshold to substantially higher levels, in order to be able to observe the onset of saturation effects. When the MCP exhibits saturation, the I_{ICD}/I_{MCP} ratio rises due to the lower I_{MCP} value. The five (I_{ICD}, I_{MCP}) data sets corresponding to the lowest I_{ICD} values, but still above the 0.2 mV I_{ICD} threshold, were used to calculate the average I_{ICD}/I_{MCP} ratio and its standard deviation. Data sets lying 2 or more standard deviations away from the average ratio were discarded. This allowed elimination of all spectra in which saturation was occurring.

2.3 RESULTS AND DISCUSSION

The major results of this study consist of the experimentally determined values for the MCP secondary electron yield γ and detection efficiency ε, for the set of 10 peptide/protein ions ranging in mass from 1 to 290 kDa, and subjected to acceleration voltages from 5 to 25 kV. These results are presented in Table 2.2; representative spectra are shown in Figure 2.2; and selected plots illustrating the important trends are shown in Figures 2.3-2.6.

2.3.1 ICD and MCP mass spectra

Figure 2.2 shows examples of typical MALDI-TOF mass spectra obtained for insulin (5729.6 Da) simultaneously from the ICD and MCP detectors at acceleration voltages from 5 to 25 kV. Important aspects of the detector responses are evident in these spectra. First, the insulin peaks (indicated by the asterisks) observed in the ICD spectra (panel a) are all similar in magnitude across the full range of acceleration voltages. This contrasts markedly with the peaks obtained from the MCP detector (panel b), which show dramatically decreased intensities at the lower acceleration voltages (compare 25kV and 5 kV in panel b). At a 5kV acceleration voltage, the two detectors have comparable sensitivity, but at higher acceleration voltages the MCP shows much better sensitivity than the ICD. In both cases the ion flight times increase at lower acceleration voltages as expected for a TOF measurement. The ICD signal also permits the number of ions that give rise to the analyte peaks in the mass spectra to be estimated: in the spectra shown in

Figure 2.2, the insulin peaks correspond to approximately 400 - 450 ions; the ion packets corresponding to the data in Table 2.2 contain 200 - 3000 ions.

2.3.2 MCP secondary electron yield

Table 2.2 shows the secondary electron yields γ for all peptides/proteins and acceleration voltages examined. The values range from somewhat greater than unity for the two smallest peptides (1.6 and 2.0 respectively for the 1 kDa angiotensin II ion and the 2.5 kDa ACTH fragment ion at 25 kV acceleration voltage) to as low as 0.013 for the 145 kDa IgG ion at 10 kV acceleration voltage. In accord with previous studies[2, 4], the results show a linear dependence of γ on ion mass, and a power law dependence on ion velocity. Figure 2.3 shows a log-log plot of the "reduced" secondary electron yield $\gamma_{red} = \frac{\gamma}{m}$ as a function of velocity, which fits well ($R^2 = 0.978$) to the power law function

$$\gamma_{red} = \frac{\gamma}{m} = 2.6 \times 10^{-18} v^{3.1} \tag{8}$$

Interestingly, the value of the velocity exponent, 3.1, differs from values of 4.3 previously reported by Westmacott *et al.*[4] and of 4.4 by our group[1], but is similar to the value of 3.2 reported by Qiao *et al.*[19] and the value of 3.3 reported for a CsI surface by Westmacott *et al.*[20] in an earlier study. These differences are likely due at least in part to the different properties of the detector surface materials, which affect both the work function and the secondary electron yield. In addition, in our previous work we employed the result of Gajewski[21], indicating that the charge induced on a conducting

ring is proportional to ion velocity; we have since determined that this relationship is not appropriate for this application, and developed the alternative analysis described in the experimental section above to obtain the velocity dependence shown. A striking feature of the plot shown in Figure 2.3 is the excellent fit obtained to this single function over four orders of magnitude in γ_{red}.

Approximating the value of the velocity exponent in equation (8) as 3.0, and combining that equation with the basic equation of TOF-MS

$$v = \sqrt{\frac{2Uze}{m}} \tag{9}$$

where U is the acceleration voltage, yields the relation

$$\gamma = 7.4 \times 10^{-18} \frac{\sqrt[\frac{3}{2}]{Uze}}{\sqrt{m}} \tag{10}$$

This shows that for a given acceleration voltage, the MCP secondary electron yield of the ions varies inversely with the square root of ion mass. Figure 2.4a shows log-log plots (γ vs m) of equation (10) for each of the five acceleration voltages. The slopes range from -0.48 (25 kV) to -0.78 (5 kV), in reasonable agreement with the value of -0.5 expected from equation (10).

2.3.3 MCP detection efficiency

Table 2.2 shows the values obtained for the MCP detection efficiency ε for all peptides/proteins and acceleration voltages examined, and plots are shown in Figure 2.4b. This parameter is very useful as it directly reports the probability that an ion will be

detected, since firing even a single MCP channel is generally sufficient for detection, in either analog or ion counting modes[22]. The values range from a high of 0.86 (2.5 kDa ACTH fragment ion at 25 kV acceleration voltage) to as low as 0.013 (the 145 kDa IgG ion at 10 kV acceleration voltage). At a 25 kV acceleration voltage, the largest protein examined, the IgG dimer at 290 kDa, is detected with 11% efficiency, corresponding to ~1 in 9 ions. It may be noted that since $e^{-\gamma} \approx 1 - \gamma$, ε also approaches γ when γ is small. The two values are almost identical for γ below 0.1. This similarity in the behavior of γ and ε is responsible for their similar behavior in the plots of Figure 2.4.

2.3.4 Effect of acceleration voltage on MCP detection

Figure 2.5 shows a plot of detection efficiency ε as a function of acceleration voltage for the set of peptides/proteins. It is notable that whereas the ion detection efficiencies vary widely at low acceleration voltage, they become much more similar at the higher acceleration voltages. This behavior reflects the fact that while low mass ions are detected with high efficiency even at low acceleration voltage, high mass ions require high acceleration voltage for efficient MCP detection. This fact has practical consequence, as it shows that high acceleration voltages are needed to efficiently detect large singly charged ions in TOF-MS, such as those generated by charge reduction of ESI-generated protein ions[23].

2.3.5 Effect of ion charge state on MCP detection

The singly and doubly charged ions of the same peptide/protein have an almost identical mass. If they are also accelerated to the same velocity, any difference in their secondary electron yields is caused by the difference in their charge state. By comparing the secondary electron yields of the singly and doubly charged ions at the same kinetic energy, the influence of the ion charge state on MCP response can be elucidated. However, as demonstrated by the bar plots in Figure 2.6 a and b, the relative secondary electron yields of $[M+H]^+$ ion and $[M+2H]^{2+}$ ion varies randomly among samples and shows no correlation with ion mass or kinetic energy. This indecisive result may be caused by the intrinsic low charge state of MALDI-generated ions. Axelsson *et al.*[24] showed that the secondary electron yield on a nonconductive surface (Al_2O_3 in this case) decreased with increasing projectile charge state by comparing the behaviors of ESI-generated albumin ions bearing 34, 44 and 55 charges. However, the extra 10 protons on the ion merely decreased the secondary electron yield by less than 10%.

2.4 CONCLUSIONS

This study comprises the most comprehensive analysis to date of MCP response to singly charged peptide/protein ions as a function of ion mass and acceleration voltage. A mass range of 1 kDa to 290 kDa was examined, 4-fold greater than previous studies, and acceleration voltages from 5 kV to 25 kV. The use of a non-destructive inductive charge detector in parallel with MCP detection provided a reliable reference signal to

allow accurate calibration of the MCP response. In accord with previous studies, the generation of secondary electrons by ion collisions is shown to vary linearly with ion mass, and as a power function with ion velocity. It is shown that for singly charged ions the secondary electron yield in a TOF experiment varies inversely with the square root of ion mass. At 25 kV acceleration voltage, all proteins are detectable, with efficiencies of ~80% for 1-2 kDa peptides, dropping to ~10% for the largest protein ion examined (IgG dimer, 290 kDa). At lower acceleration voltages, detection efficiency is significantly reduced in all cases, and the larger proteins become undetectable. The influence of the ion charge state on MCP detection efficiency is not significant for the MALDI-generated ions.

REFERENCES

1. Chen, X., Westphall, M.S., Smith, L.M. Mass Spectrometric Analysis of DNA Mixtures: Instrumental Effects Responsible for Decreased Sensitivity with Increasing Mass. *Anal. Chem.* **75**(21), 5944-5952 (2003).

2. Geno, P.W., Macfarlane, R.D. Secondary electron emission induced by impact of low-velocity molecular ions on a microchannel plate. *Int. J. Mass Spectrom.* **92**, 195-210 (1989).

3. de Hoffmann, E., Stroobant, V. Mass Spectrometry Principles and Applications, 3rd ed. John Wiley & Sons: Chicester, U.K. (2007).

4. Westmacott, G., Frank, M., Labov, S.E., Benner, W.H. Using a superconducting tunnel junction detector to measure the secondary electron emission efficiency for a microchannel plate detector bombarded by large molecular ions. *Rapid Commun. Mass Spectrom.* **14**(19), 1854-1861 (2000).

5. Tran, J.C., Zamdborg, L., Ahlf, D.R., Lee, J.E., Catherman, A.D., Durbin, K.R., Tipton, J.D., Vellaichamy, A., Kellie, J.F., Li, M., Wu, C., Sweet, S.M., Early, B.P., Siuti, N., LeDuc, R.D., Compton, P.D., Thomas, P.M., Kelleher, N.L. Mapping intact protein isoforms in discovery mode using top-down proteomics. *Nature*. **480**(7376), 254-258 (2011).

6. Hilton, G.C., Martinis, J.M., Wollman, D.A., Irwin, K.D., Dulcie, L.L., Gerber, D., Gillevet, P.M., Twerenbold, D. Impact energy measurement in Time-of-Flight mass spectrometry with cryogenic microcalorimeters. *Nature*. **391**(6668), 672-675 (1998).

7. Wenzel, R.J., Matter, U., Schultheis, L., Zenobi, R. Analysis of megadalton ions using cryodetection MALDI Time-of-Flight mass spectrometry. *Anal. Chem.* **77**(14), 4329-4337 (2005).

8. Park, J., Qin, H., Scalf, M., Hilger, R.T., Westphall, M.S., Smith, L.M., Blick, R.H. A mechanical nanomembrane detector for Time-of-Flight mass spectrometry. *Nano Lett.* **11**(9), 3681-4 (2011).

9. Contino, N.C., Pierson, E.E., Keifer, D.Z., Jarrold, M.F. Charge detection mass spectrometry with resolved charge states. *J. Am. Soc. Mass Spectrom.* **24**(1), 101-108 (2013).

10. Fuerstenau, S.D., Benner, W.H. Molecular weight determination of megadalton DNA electrospray ions using charge detection Time-of-Flight mass spectrometry. *Rapid Commun. Mass Spectrom.* **9**(15), 1528–1538 (1995).

11. Fuerstenau, S.D., Benner, W.H., Thomas, J.J., Brugidou, C., Bothner, B., Siuzdak, G. Mass Spectrometry of an Intact Virus. *Angew. Chem. Int. Ed.* **40**(3), 541-544 (2001).

12. Doussineau, T., Kerleroux, M., Dagany, X., Clavier, C., Barbaire, M., Maurelli, J., Antoine, R., Dugourd, P. Charging megadalton poly(ethylene oxide)s by electrospray ionization. A charge detection mass spectrometry study. *Rapid Commun. Mass Spectrom.* **25**(5), 617-623 (2011).

13. Keifer, D.Z., Pierson, E.E., Hogan, J.A., Bedwell, G.J., Prevelige, P.E., Jarrold, M.F. Charge detection mass spectrometry of bacteriophage P22 procapsid distributions above 20 MDa. *Rapid Commun. Mass Spectrom.* **28**(5), 483-488 (2014).

14. Benner, W.H., Bogan, M.J., Rohner, U., Boutet, S., Woods, B., Frank, M. Non-destructive characterization and alignment of aerodynamically focused particle beams using single particle charge detection. *J. Aero. Sci.* **39**(11), 917-928 (2008).

15. Smith, J.W., Siegel, E.E., Maze, J.T., Jarrold, M.F. Image charge detection mass spectrometry: pushing the envelope with sensitivity and accuracy. *Anal. Chem.* **83**(3), 950-956 (2011).

16. Beuhler, R.J., Friedman, L. Low noise, high voltage secondary emission ion detector for polyatomic ions. *Int. J. Mass Spectrom.* **23**(2), 81-97 (1977).

17. Fraser, G.W., Pain, M.T., Lees, J.E., Pearson, J.F. The operation of microchannel plates at high count rates. *Nucl. Instrum. Meth. A.* **306**(1-2), 247-260 (1991).

18. Cleveland, W.S. Robust Locally Weighted Regression and Smoothing Scatterplots. *J. Am. Stat. Assoc.* **74**(368), 829-836 (1979).

19. Qiao, H., Collado, V., Piyadasa, G., Loboda, A., Kozlovski, V., Spicer, V., Standing, K.G., Ens, W. Comparison of electron and ion emission efficiencies in a hybrid detector in an orthogonal TOF instrument. in 53rd American society for mass spectrometry annual conference. 2005. San Antonio, TX.

20. Westmacott, G., Ens, W., Standing, K.G. Secondary ion and electron yield measurements for surfaces bombarded with large molecular ions. *Nucl. Instrum. Meth. B.* **108**(3), 282-289 (1996).

21. Gajewski, J.B. Mathematical model of non-contact measurements of charges while moving. *J. Electrostat.* **15**(1), 81-92 (1984).

22. Wiza, J.L. Microchannel plate detectors. *Nucl. Instrum. Meth. A*. **162**, 587-601 (1979).

23. Scalf, M., Westphall, M.S., Smith, L.M. Charge Reduction Electrospray Mass Spectrometry. *Anal. Chem.* **72**(1), 52-60 (1999).

24. Axelsson, J., Reimann, C.T., Sundqvist, B.U.R. Secondary electron emission from surfaces impacted by multiply-charged polyatomic ions. *Nucl. Instrum. Meth. B*. **88**(1-3), 131-137 (1994).

Table 2.1 Peptide/protein standards

peptides/proteins	molecular weight (Da)
angiotensin II	1045.5
ACTH fragment	2464.2
insulin	5729.6
cytochrome c	12361
apomyoglobin	16951
aldolase	39211
albumin	66429
phosphorylase b	97,200
IgG	145,000

Table 2.2 Data summary showing the measured velocity v, secondary electron yield γ and detection efficiency ε for the 10 peptide/protein ions at various acceleration voltages.

peptide/protein (ion mass)	acceleration voltage (kV)	v (km/s)	γ	γ/m	ε	peptide/protein (ion mass)	acceleration voltage (kV)	v (km/s)	γ	γ/m	ε
angiotensin II (1046.5 Da)	25	68	1.6	1.5E-03	0.79	aldolase (39212 Da)	25	11	0.31	7.9E-06	0.27
	20	61	1.4	1.3E-03	0.74		20	9.7	0.27	6.9E-06	0.24
	15	53	1.5	1.5E-03	0.78		15	8.4	0.26	6.7E-06	0.23
	10	43	1.2	1.1E-03	0.69		10	6.8	0.14	3.6E-06	0.13
	5	30	0.49	4.7E-04	0.39		5	4.8	0.023	5.9E-07	0.023
ACTH fragment (2465.2 Da)	25	44	2.0	7.9E-04	0.86	albumin (66430 Da)	25	8.3	0.30	4.5E-06	0.26
	20	39	0.83	3.4E-04	0.56		20	7.5	0.30	4.5E-06	0.26
	15	34	1.1	4.6E-04	0.68		15	6.4	0.21	3.2E-06	0.19
	10	28	0.40	1.6E-04	0.33		10	5.2	0.079	1.2E-06	0.076
	5	20	0.11	4.5E-05	0.10		5	3.6	0.0088	1.3E-07	0.0087
insulin (5730.6 Da)	25	29	1.4	2.4E-04	0.74	phosphorylase b (97.2 kDa)	25	6.9	0.29	2.9E-06	0.25
	20	26	1.1	1.9E-04	0.66		20	6.2	0.26	2.7E-06	0.23
	15	22	0.54	9.5E-05	0.42		15	5.3	0.16	1.7E-06	0.15
	10	18	0.22	3.9E-05	0.20		10	4.3	0.037	3.8E-07	0.036
	5	13	0.051	8.9E-06	0.050		5	-	-	-	-
cytochrome c (12362 Da)	25	19	0.69	5.6E-05	0.50	IgG (145 kDa)	25	5.6	0.28	1.9E-06	0.24
	20	17	0.48	3.9E-05	0.38		20	5.0	0.17	1.2E-06	0.16
	15	15	0.32	2.6E-05	0.28		15	4.3	0.077	5.3E-07	0.074
	10	12	0.16	1.3E-05	0.15		10	3.5	0.013	9.3E-08	0.013
	5	8.6	0.086	6.9E-06	0.082		5	-	-	-	-
apomyoglobin (16952 Da)	25	17	0.44	2.6E-05	0.36	IgG [2M+H] (290 kDa)	25	4.0	0.12	4.1E-07	0.11
	20	15	0.32	1.9E-05	0.27		20	3.5	0.052	1.8E-07	0.052
	15	13	0.29	1.7E-05	0.25		15	-	-	-	-
	10	10	0.15	8.7E-06	0.14		10	-	-	-	-
	5	7.4	0.070	4.1E-06	0.068		5	-	-	-	-

- indicates signal on one or both detectors is below limit of detection.

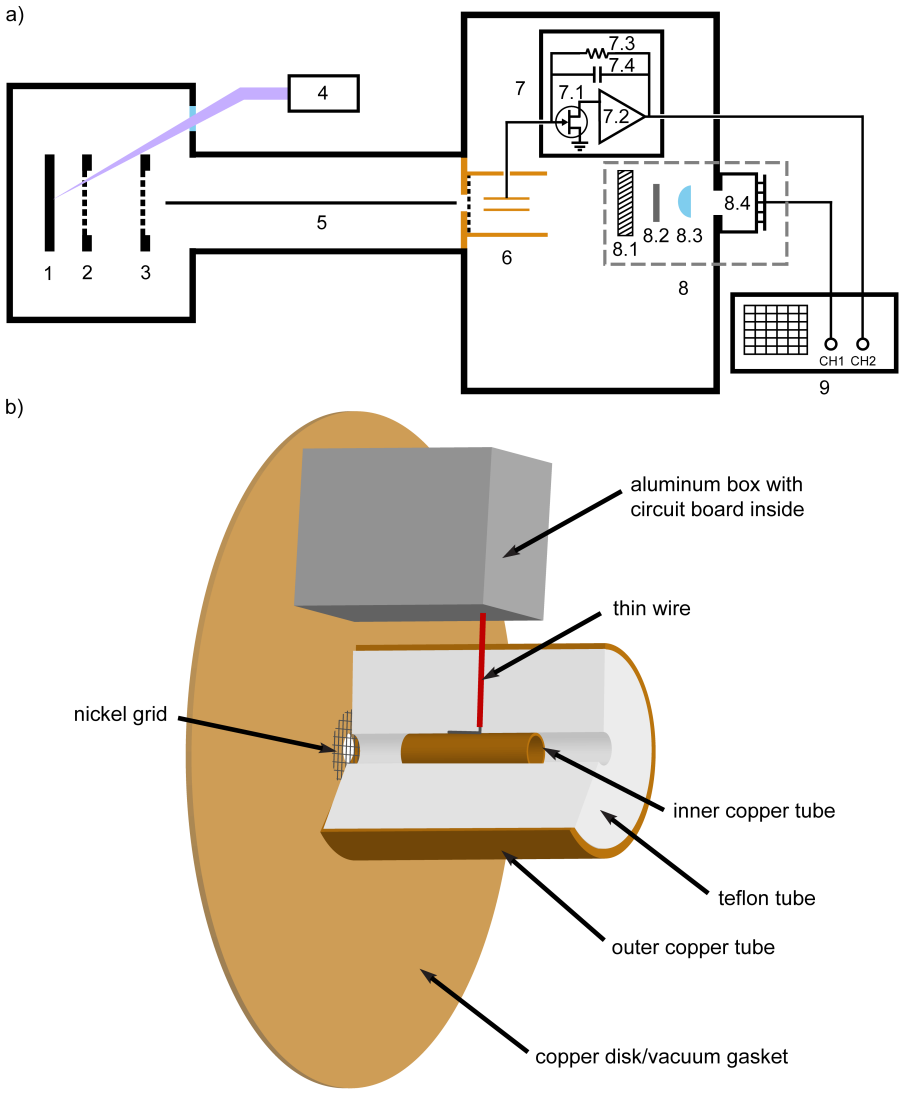

Figure 2.1 a) Instrument schematic diagram showing the MALDI mass spectrometer with two detectors. 1: sample plate. 2: variable-voltage grid. 3: ground grid. 4: nitrogen laser. 5: guide wire. 6: ICD. 7: ICD circuit board. 7.1: 2SK152 FET. 7.2: A250 charge-sensitive preamplifier. 7.3: 1 GΩ feedback resistor. 7.4: parasitic capacitance shown as a symbolic feedback capacitor. 8: high current detector (HCD). 8.1: MCP. 8.2: scintillator. 8.3: focusing lens. 8.4: photosensor module with attached circuit board. 9: oscilloscope. b) Expanded view of the ICD assembly, components 6 and 7.

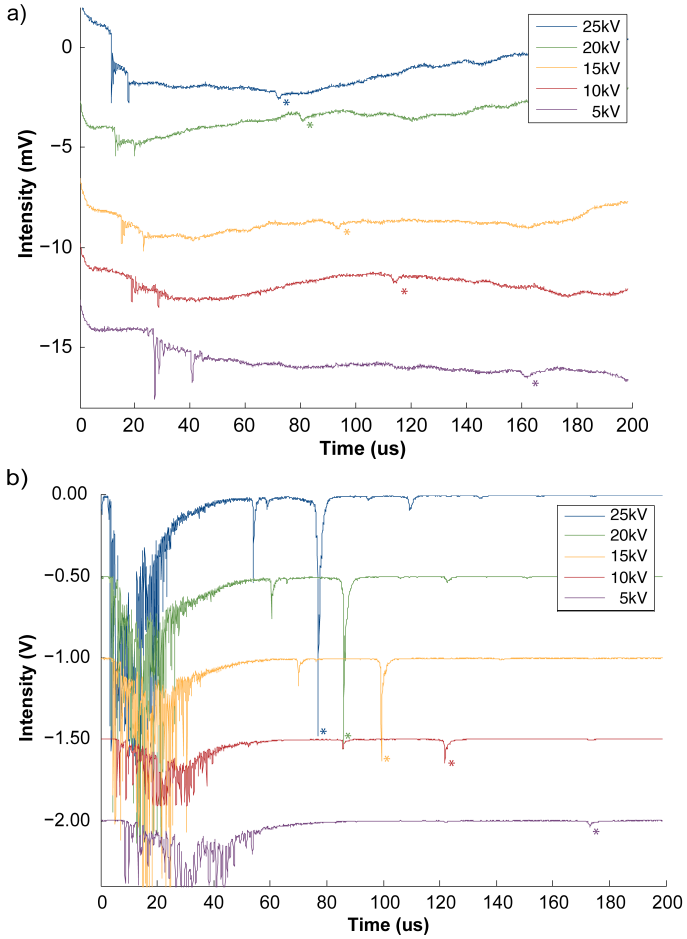

Figure 2.2 Comparison of insulin MALDI spectra acquired with the ICD (a) and MCP detector (b) at different acceleration voltages. $[M+H]^+$ peaks are denoted with an asterisk. Peak heights in the ICD spectra are all of comparable magnitudes, while peak heights in the MCP spectra vary by ~50 fold. The mass spectra corresponding to acceleration voltages of 20 to 5 kV are offset vertically from the 25 kV spectrum by -5 mV increments in a) and -0.5 V increments in b) to create a stacking view. Matrix peaks (those peaks occurring before ~50 μsec) in the 10 kV and 5 kV spectra in b) were truncated during data acquisition due to the oscilloscope setting employed to expand the low intensity analyte peaks.

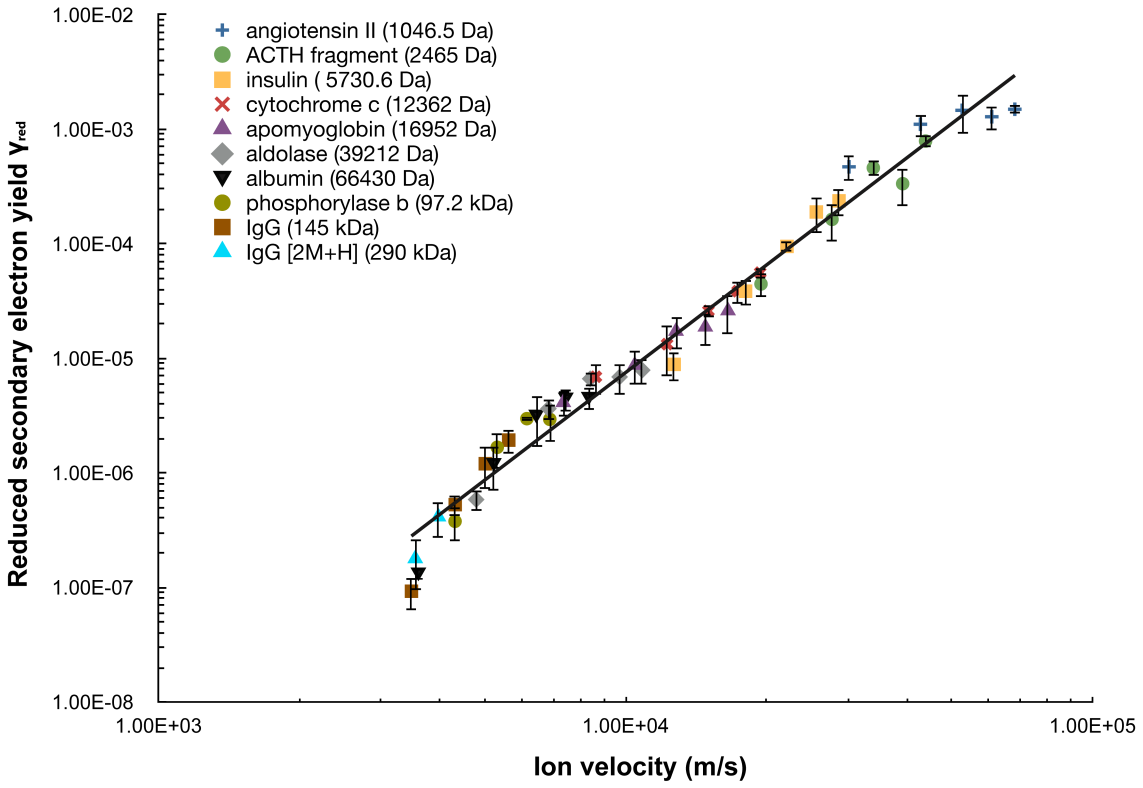

Figure 2.3 Reduced secondary electron yield γ_{red} of the MCP detector for 10 peptide/protein ions plotted as a function of ion velocity. Note that multiple ion velocity data points are present for each peptide/protein due to the various acceleration voltages employed. All ions are $[M+H]^+$ ion except for the singly charged dimer of IgG. The solid line is a power law fit to the data with the function $\gamma_{red} = \frac{\gamma}{m} = 2.6\times10^{-18} v^{3.1}$ ($R^2 = 0.978$). Error bars correspond to ± 1 standard deviation.

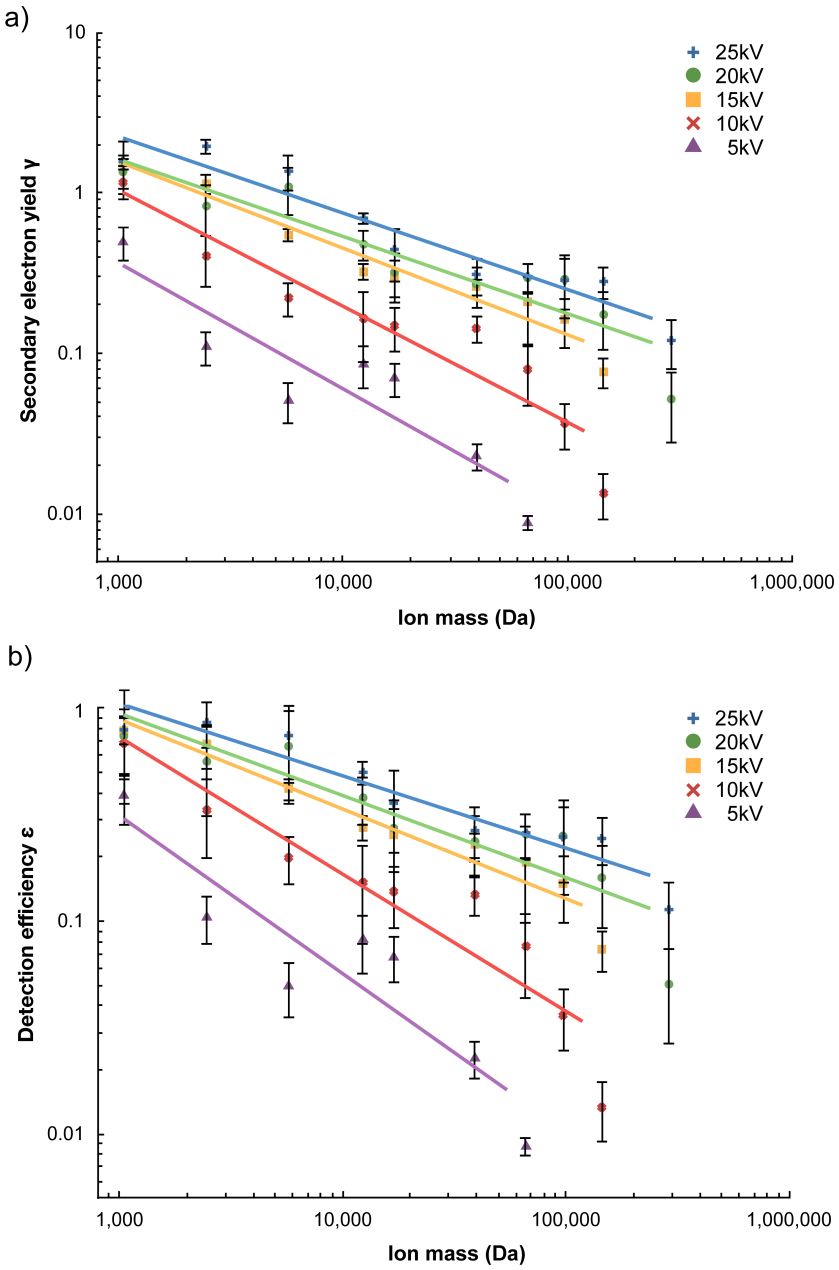

Figure 2.4 MCP secondary electron yield γ (a) and detection efficiency ε (b) plotted as a function of ion mass. At each acceleration voltage, the data is fit to a power law function as indicated by the solid lines. Error bars correspond to ± 1 standard deviation.

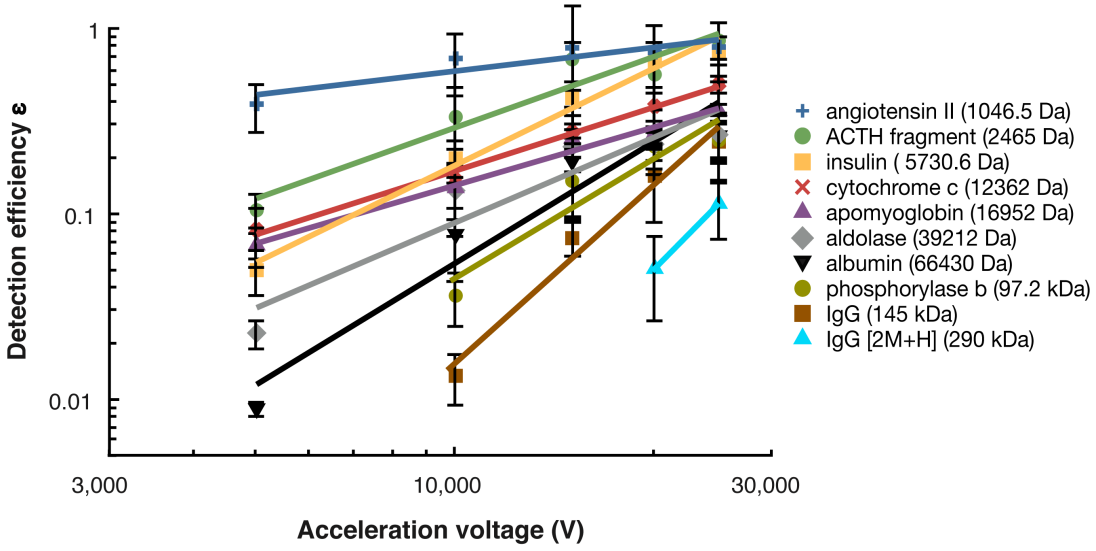

Figure 2.5 MCP detection efficiency ε plotted as a function of acceleration voltage. For each peptide/protein ion, the data is fit to a power law function as indicated by the solid lines. Error bars correspond to ± 1 standard deviation.

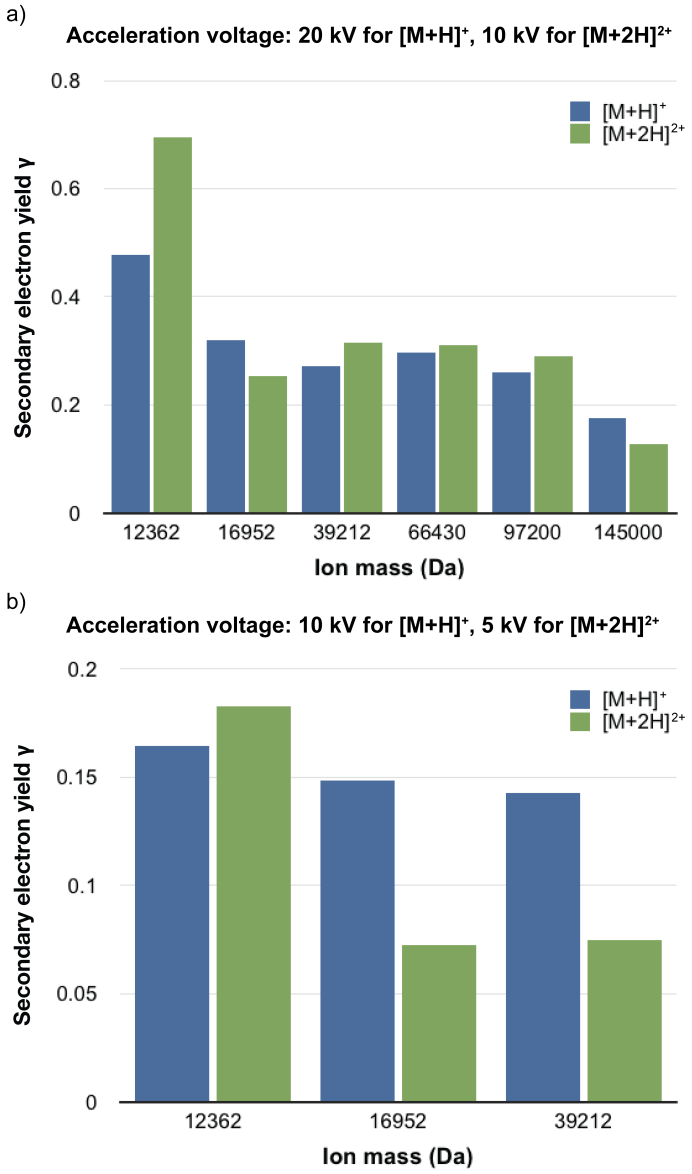

Figure 2.6 MCP secondary electron yields γ of singly and doubly charged ions at 20 keV (a) and 10 keV (b).

CHAPTER 3

The Influence of Nanomembrane Composition, Ion Mass, and Acceleration Voltage on Ion Detection with Nanomembrane Detectors in Time-of-Flight Mass Spectrometry

3.1 INTRODUCTION

Microelectromechanical systems (MEMS) are microscopic mechanical machines that have been developed and characterized for decades. Some are deployed in commercial applications in our daily lives including inkjet printers, accelerometers and a variety of sensors[1]. With the advances in nanofabrication technologies, MEMS are pushed into the nano-scale and nanoelectromechanical systems (NEMS) have emerged in recent years[2]. The distinctive small dimensions of NEMS provide exceptional sensitivity when serving as nanomechanical sensors[3]. Their applications range from gas detection to label-free biological detection[4]. One type of nanomechanical sensor is able to measure a very small mass change on a cantilever when analyte molecules are adsorbed onto it[5]. The mass resolution of the nanomechanical sensors decreases with the mass of the cantilever and minimum values of ~25 zg (1 zg = 10^{-21} g) at room temperature and ~1 zg at 5 K have been achieved[6]. Utilization of such sensors in mass spectrometry (MS),

prompted by Roukes *et al.* as NEMS MS[7], broadens the horizons of mass spectrometry with an extremely sensitive approach for large biomolecule analysis without the necessity of sample ionization. However, the practical implementation requires a much larger active sensing area and an efficient transfer of the uncharged analyte molecules to the detector.

We have developed a mechanical nanomembrane detector for ion detection in Time-of-Flight (TOF) mass spectrometry as shown in Figure 3.1[8]. The primary element of the detector is a freestanding nanomembrane with an exceptionally large surface area to volume ratio. Due to a high voltage applied between the nanomembrane and the extraction grid, the nanomembrane emits electrons, which is a phenomenon called field emission[9]. The electrons are amplified by two microchannel plates (MCPs) and collected by the anode. When ions impinge on the nanomembrane, their kinetic energy is transferred to the nanomembrane and causes the temperature in the vicinity of the impact site to rise. Depending on the composition of the nanomembrane, the dissipation of this extra thermal energy occurs by different routes. In the case of an Al-coated Si_3N_4 nanomembrane[8, 10], the temperature gradient leads to thermomechanical forces, resulting in mechanical deformation and vibrations of the nanomembrane. As the distance between the nanomembrane and the grid varies during vibration, the field emission current oscillates at the same frequency. In the case of a Si nanomembrane[11, 12], the electrons are excited to higher energy states by the non-equilibrium phonons and

thus are able to overcome the vacuum barrier. Subsequently, an increased number of electrons escape from the nanomembrane and cause a spike in field emission current.

The nanomembrane detector responses to ion's kinetic energy that is determined by acceleration voltage and ion charge state in TOF-MS. The detector response should be independent of ion mass, which, if is true, will make the nanomembrane detector very promising for large protein ion detection. A thorough characterization of the detector response is carried out here. We measured the characteristic field emission curves for different nanomembranes and compared their performance using 9 peptides/proteins in a MALDI-TOF instrument. Acceleration voltage was varied between 5 and 25 kV to evaluate the sensitivity of each nanomembrane.

3.2 EXPERIMENTAL

3.2.1 Nanomembrane fabrication

Most nanomembranes were fabricated by Christina Lampe and Jana von Poblotzki from the Blick research group in the University of Hamburg except for the Al-coated ones that were fabricated by Hyunseok Kim in the University of Wisconsin-Madison. A thin layer of silicon nitride (Si_3N_4) was deposited on both sides of a 400 μm thick Si wafer (100) by low-pressure chemical vapor deposition (LPCVD). Then the Si wafer was cut into 10 mm × 10 mm square pieces. After both sides were protected with photoresist, a window defining the freestanding region of the nanomembrane was created on the backside by photolithography. The backside Si_3N_4 layer within the window was

removed by reactive-ion etching (RIE). After cleaning off the photoresist with acetone, the Si wafer in the window is etched away by either warm KOH solution for square nanomembranes or by plasma etching for round nanomembranes. Finally, a thin metal layer was deposited on the front side, or both sides, by atomic layer deposition (ALD) for the 500 nm thick Pt-coated nanomembranes, or by sputtering deposition for all others. The compositions and dimensions of all nanomembranes are provided in Table 3.1. They can be divided into two groups, relatively thick (500 nm) nanomembranes (the first and the second ones in Table 3.1) and relatively thin (30 nm and 50 nm) nanomembranes. One of each type of the thick nanomembrane and multiple thin nanomembranes were fabricated. Pictures of three different nanomembranes are shown in Figure 3.2a.

3.2.2 Field emission current measurement

The device for measuring the field emission current from the nanomembrane is illustrated in Figure 3.2b. It consists of four parts: a copper holder (1.50" in diameter and 0.125" thick), an insulating polyimide spacer (1.60" in diameter), a nickel grid bonded on a frame (1.50" in diameter and 0.125" thick) and a stainless steel anode (1.00" in diameter and 0.060" thick). As shown in Figure 3.2c, the holder had a 5 mm×5 mm opening and a 10 mm×10 mm recess at the center, in which the nanomembrane was placed and attached using colloidal silver paste (Ted Pella, Redding, CA). Silver paste was applied to both sides of the nanomembrane to make a good electric connection between the holder and the metal layer. The spacer was 0.003" or 0.005" in thickness with a square hole

slightly larger than the freestanding region. The electroformed nickel grid had 70 wires per inch and a maximum transmission of 90% (Precision Eforming LLC, Cortland, NY). It was tightly bonded to the stainless steel frame, forming a flat and rigid mesh on the 7 mm × 7 mm opening on the frame. Six nylon screws held the holder and the frame tightly together through holes near the rim so the distance between the nanomembrane and the grid was approximately defined by the spacer thickness.

Nanomembrane voltage (V_{NM}) and grid voltage (V_G) were applied to the nanomembrane holder and grid frame via separate wires. Voltages were manually ramped carefully following an optimized procedure for each nanomembrane. First, both voltages were gradually increased until reaching -300 V. Such voltage applied to the grid directs the electrons from the grid to the anode. Then the nanomembrane voltage was increased at a rate of -5 V per 5 s when a 0.005" thick spacer was used or -3 V per 5 s for a 0.003" thick spacer. After every -100 V, ramping was paused for 15 to 30 s to allow the nanomembrane to reach an equilibrium state under that electric field. Nanomembrane voltage was continuously increased until either the nanomembrane broke or a prominent field emission current was observed. The anode was placed 3 mm away from the frame to collect the emitted electrons. The field emission current was amplified by a variable-gain low-noise current amplifier (DLPCA-200, Electro optical components, Santa Rosa, CA) at a gain of 10^9 V/A, which was then digitized by a Tektronix CDM250 digital multimeter at a rate of 2.5 Hz. All measurements were performed in a vacuum below 5×10^{-7} Torr.

Field emission current I from the nanomembrane can be approximately described by the Fowler-Nordheim equation[9] in the form of

$$I = AF^2 e^{-\frac{B}{F}} \quad (1)$$

where F is the electric field between the nanomembrane and the grid; A and B are parameters related to the work function of the material, namely the minimum thermodynamic work or energy needed to remove an electron from a solid to a point in the vacuum immediately outside the solid surface. The work function of a material can be obtained from the slope and intercept of the fitted curve in a Fowler-Nordheim plot where $\ln(\frac{I}{F^2})$ is plotted against $\frac{1}{F}$. If the distance between the nanomembrane and extraction grid is constant, F is calculated from the voltage difference ($V = V_{NM} - V_G$) and the spacer thickness (d) as $\left|\frac{V_{NM} - V_G}{d}\right|$, which can be simply replaced by V. However, the nanomembrane bends toward the grid due to the electrostatic force, resulting in a smaller gap and a stronger electric field.

3.2.3 Ion detection with nanomembrane detectors in a MALDI-TOF instrument

MALDI samples were prepared in the same way as in Chapter 2. Experiments were performed on the same Voyager DE STR mass spectrometer described in Chapter 2 and all acquisition parameters remained unchanged. The inductive charge detector (ICD) was installed but not functioning in these measurements. The ICD has an inner diameter of 5 mm, tailoring the ion packet to the same diameter to match the size of the

nanomembrane. The nanomembrane detector, including a nanomembrane, a spacer and an extraction grid, were mounted on a magnetic sample transporter (MCD Vacuum products LLC, Hayward, CA) in the last section of the fight tube between the ICD and the MCP detector. The freestanding region of the nanomembrane was in the center of the ion path. Nanomembrane voltage and grid voltage were varied during the measurements based on the signal intensity and also the previously measured field emission curve of the specific nanomembrane. In general, grid voltage was increased to a higher value between -500 V to -800 V, so that the electrons were more energetic and could generate a higher signal on the MCP detector placed 5 mm downstream of the grid. The output signal from the MCP detector was monitored with a Tektronix DPO 2024B oscilloscope (Tektronix, Beaverton, OR) in AC coupling mode, thus only transmitting the current fluctuations caused by ion bombardment. Each mass spectrum obtained was an average of signals from 8 laser shots. Mass spectra of samples can also be acquired with the MCP detector directly, which was realized by moving the nanomembrane detector out of the ion path using the magnetic sample transporter.

3.3 RESULTS AND DISCUSSION

Out of 40 nanomembranes examined in this study in total, only three nanomembranes gave a stable field emission current whereas the others broke during voltage ramping. Two out of these three nanomembranes survived the field emission measurement and were successfully employed for ion detection. The field emission curves

and selected spectra are shown below, and the ion detection mechanisms of different nanomembranes are discussed.

3.3.1 500 nm thick Pt-coated Si_3N_4 nanomembranes in a 4 by 4 array

The data presented below were obtained from a 4 by 4 array of 500 nm thick Si_3N_4 nanomembranes with a 15 nm thick Pt coating on both sides, each of which was 1 mm in diameter. A 0.003" thick spacer was used in all experiments, which covered the twelve outer nanomembranes in the array (that were partially concealed by the grid frame anyway) as well as a broken nanomembrane in the center. This resulted in a total freestanding area of 2.4 mm^2, which is about 10% of that of the 5 mm × 5 mm nanomembrane.

Field emission. Three measurements of field emission current were performed in series at intervals of 10 min. The results are presented in an I-V plot (Figure 3.3a) and a Fowler-Nordheim plot (Figure 3.3b). The three I-V curves are quite similar in general. Field emission current starts to increase after the voltage difference reaches 1400 V, and finally takes off after 1520 V. The turn-on voltages are defined here as the voltage difference where the current exceeds 100 pA, are 1561 V, 1555 V and 1529 V in the three measurements respectively. The field emission current above 1530 V can be approximately described by the Fowler-Nordheim equation as shown in Figure 3.3b. Voltage difference is directly used in the Fowler-Nordheim plot for simplicity, which is justified by the good linearity of the fitting curves. However, the field emission is very

unstable, introducing high uncertainties to the fitted Fowler-Nordheim equations and preventing accurate determination of the work function.

The decreasing turn-on voltage with each new measurement indicates that field emission happens more readily. This trend is clearly evident in the Fowler-Nordheim plot. The number of electrons emitted from the nanomembranes is almost always higher in the latter measurement at the same voltage difference, causing the fitted line to shift upward. It is possible that the nanomembranes tend to buckle to a greater extent in the latter measurements, and more electrons are emitted consequently due to a stronger electric field. Based on this assumption, the distance between the nanomembranes and the grid is calculated to be only 1% less in the second measurement and 2% less in the third measurement compared with that in the first measurement. In general, the field emission from the nanomembrane is reproducible.

Ion detection. While employing this nanomembrane for protein ion detection, V_{NM} and V_G were set to -2100 V and -500 V, respectively during all measurements. This 1600 V difference should produce at least 3300 pA base current, as predicted by the fitted Fowler-Nordheim equation obtained from the last field emission measurement.

Successful detection of protein ions occurred with this nanomembrane detector under certain conditions. Specifically, the highest acceleration voltage (25 kV) and high laser intensities (15% to 25% higher than the maximum intensities that won't cause MCP saturation) were required, which means this nanomembrane detector only responded to compact and high-energy ion packets. The low sensitivity of the nanomembrane array

may be attributed to its thickness and small active area. If ions in each ion packet are evenly distributed, then only 12% of the ions passing through the inductive charge detector collide on the nanomembrane. Angiotensin II, ACTH fragment and aldolase failed to be detected probably due to the low abundance of protein ions in the ion packet. Selected mass spectra of other proteins are shown in Figure 3.4 and the known protein ion peaks are labeled. Almost all peaks in the spectra are extremely narrow with a width around 200 ns, resulting in a high resolution ($m/\Delta m$) that increases with ion mass. The resolution of the IgG $[M+H]^+$ peak reaches 2000. Random spikes similar to protein peaks appear across the whole spectrum especially at high laser intensities, suggesting the existence of fragment ions produced at these high laser intensities. However, they also appear in the matrix spectra as shown in Figure 3.5. We believe the spikes are thus more likely to be caused by electronic noise. From Figure 3.5 we can see that the matrix peaks grow in both number and height when laser intensity increases, which means the detector response increases with the number of ions in each ion packet.

The peak shape is shown by the enlarged insulin and cytochrome c $[M+H]^+$ peaks in the insets of Figure 3.4, from which we can see that the field emission current rises up rapidly to a plateau upon ion collision and then gradually falls back to the baseline through an exponential decay. The length of the plateau is around 50 ns and the decay rate is constant. This unique peak shape indicates a novel ion detection mechanism specific to this type of nanomembrane. Although not yet well understood, the detection mechanism is possibly similar to that of the Si nanomembrane, as mentioned in the

Introduction to this chapter. Upon collision, the kinetic energy of the ions is transferred to the nanomembrane. This raises the temperature in the vicinity of the collision and produces non-equilibrium phonons that quickly reach the front surface of the nanomembrane. Some electrons are excited by the phonons to higher energy states that are prone to tunnel through the surface barrier into vacuum, which results in a sudden upsurge in the field emission current. Since both Si_3N_4 and Pt are comparatively low in thermal conductivity (Si_3N_4: 16-33 $Wm^{-1}K^{-1}$, Pt: 71.6 $Wm^{-1}K^{-1}$, Si: 124 $Wm^{-1}K^{-1}$[13]) and the nanomembrane is quite thick, the thermal energy is confined to the vicinity of the collision for a short period of time before starting to diffuse. The heat is then carried away by phonons travelling laterally on the surface of the nanomembrane. The characteristic decay rate of the field emission current is determined by the lateral velocity of the phonons. When the phonon energy falls below a threshold as the thermal energy is released, no more electrons are excited and the field emission current returns to the baseline.

3.3.2 30 nm thick Si_3N_4 nanomembrane with a 15 nm Au coating on both sides

The 30 nm thick Si_3N_4 nanomembrane with a 15 nm Au coating on both sides has an area of 5 mm × 5 mm. With such a high surface area to volume ratio, the nanomembrane deformation caused by the strong electric force is significant and sometimes tears up the nanomembrane. We believe that this is the main reason for the low survival rate of the relatively thin (30 and 50 nm) nanomembranes. Nonetheless, we

were able to acquire field emission from two of these nanomembranes and protein detection data from one of them.

Field emission. The field emission current was first measured with a 0.005" spacer. As shown in Figure 3.6, the current emerges at 1410 V and shoots up quickly after 1590 V to the turn-on voltage of 1610 V. However, the nanomembrane broke after the measurement was complete. A second measurement was taken on a new nanomembrane with a 0.003" spacer. This time current appears at 1005 V and the turn-on voltage is 1055 V (curve not shown here).

Under the same electric field, the deformations of the nanomembrane are presumably similar. As mentioned before, the bending of the nanomembrane towards the grid increases the strength of the electric field. The resulting enhancement to field emission is greater in the case of a thinner spacer because of a shorter remaining distance. As a consequence, the field emission should occur at a lower electric field and the current should rise more rapidly when a thinner spacer is present. However, our observations only partially agree with this theory. In the second measurement, when a thinner spacer was used, the electric field is stronger when the field emission first occurs but the field emission is turned on much sooner. This can be attributed to the variations in the nanomembranes as well as in the detector assembly process.

During the second measurement, instability of the nanomembrane under the strong electric field was observed, which is clearly revealed with the field emission current plotted against time in Figure 3.7. The field emission current was steady around 4 pA

from 1035 V to 1050 V. When the voltage difference was increased to 1055 V, the current stayed at around 13 pA for about 5 s and suddenly soared. The nanomembrane probably underwent a large deformation due to the tension brought about by the abrupt electric field change. In the following 35 s, the nanomembrane didn't reach an equilibrium position and the current oscillated around 97 pA. After the voltage difference was reduced back to 1050 V, the current dropped gradually to 24 pA. Compared to the first time when the voltage difference attained 1050 V, the current was 6 times higher and fluctuated more, indicating that the nanomembrane did not restore itself to the original equilibrium position, maybe because of residual strains. Afterwards, the nanomembrane voltage was ramped at a lower rate (2 V increments), therefore the current increased at a steadier pace and the change in nanomembrane shape was very subtle. The field emission was finally turned on again after the voltage difference stayed at 1058 V for a couple of seconds. In conclusion, the voltage ramping rate influences nanomembrane deformation and thus field emission current. A delay exists between voltage change and nanomembrane bending. Overall, the field emission current is unstable as the electric field gets stronger.

Ion detection. The second nanomembrane with the same 0.003" spacer was then used for ion detection. Only angiotensin II and ACTH fragment samples could be detected with this nanomembrane detector. Figure 3.8a is the first ACTH fragment mass spectrum obtained at a V_{NM} of -1730 V and a V_G of -700 V, corresponding to a 2.5 pA base current calculated from the field emission measurement result. Despite the noisy

background, the ACTH fragment $[M+H]^+$ peak has a S/N of 20 and even the doubly charged ion peak is above the detection limit. Figure 3.8b was acquired after bringing both V_{NM} and V_G up by 100 V, intending to increase the kinetic energy of the field emitted electrons for a higher amplification on the MCP detector. The spectrum shows a 30% growth of the $[M+H]^+$ peak as well as a boost in noise level, so the S/N remains unchanged. In Figure 3.8c, the voltage difference is increased to 1040 V (the base current increases to 4 pA) but no improvement on the spectrum can be observed. Note that the laser intensities in Figure 3.8 a to c are all 54.3% of the full power. With the laser intensity reduced to 52.2%, less protein ions are generated that are barely detectable (Figure 3.8d), suggesting the ion quantity, or to be more exact, the total energy of the ion packet, needs to exceed a certain threshold to activate the nanomembrane detector.

A mass spectrum of the ACTH fragment sample was obtained on the MCP detector directly for a semi-quantitative measurement of the protein ion quantity at laser intensity of 54.3%. As shown in Figure 3.8e, the $[M+H]^+$ peak intensity is 10 times of those in the nanomembrane detector spectra. Given the vast amount of matrix ions continuously striking the MCP from 2 μs to 30 μs after each laser shot, the MCP is saturated when the ACTH fragment ion packet arrives, which means the $[M+H]^+$ peak should be even higher. The detection efficiency of an ion on the MCP detector is determined by the secondary electron yield γ, i.e. the average number of electrons produced per ion collision. The 25 keV ACTH fragment ion has a yield of 2.0 as measured in Chapter 2. Similarly, the detection efficiency of the nanomembrane detector

can be represented by the field emission electron yield, i.e. the average number of electrons emitted from the nanomembrane per ion collision. Assuming every field emitted electron will produce 1 secondary electron on the MCP detector, which is reasonable given the high speed of those electrons, then the electron yield of each ACTH fragment ion on the nanomembrane is about 0.16, which is comparable to the secondary electron yield of IgG $[2M+H]^+$ ions at 25 keV (γ = 0.12 measured with the MCP detector in Chapter 2). So the nanomembrane detector efficiency is much lower than that of the MCP detector.

Since the nanomembrane detector is activated by the energy transferred from ions, its response depends on the total kinetic energy of an ion packet. At a voltage difference of 1040 V, the ACTH fragment ion can be detected using 50.0% of the full laser power at a 25 kV acceleration voltage (Figure 3.8f) but not at any lower acceleration voltages. For low energy ions, higher laser intensity is required to produce more ions and compensate for the reduced total energy. When the laser intensity is increased to 51.1%, both 20 keV and 15 keV ACTH fragment ions are detected (Figure 3.8 g and h) but the latter has a significantly lower peak height. However, when the acceleration voltage is further decreased to 10 kV and 5 kV, detection failed at even higher laser intensities. The same trend is also shown in the series of angiotensin II spectra (Figure 3.9) acquired at different acceleration voltages under the same condition (Laser is at 50.0% of full power. V_{NM} is -1740 V and V_G is -700 V.). The $[M+H]^+$ peak intensity and S/N decrease with the ion's kinetic energy.

The expanded angiotensin II $[M+H]^+$ peaks are included in Figure 3.9 as insets. Each peak is symmetric and about 0.4 μs wide. The Gaussian peak profile is probably determined by the axial distribution of the ions in the ion packet. When an ion packet reaches the nanomembrane, the energy transferred from the ions accumulates on the nanomembrane and finally some electrons acquire enough energy to overcome the barrier and escape into vacuum. Under the continuous striking of an increasing number of ions onto the nanomembrane, the field emission current keeps rising. At the same time, due to the high thermal conductivity of gold (317 $Wm^{-1}K^{-1}$[13]), the thermal energy is released very quickly. Therefore, after the majority of the ions have arrived, the field emission current decreases.

As mentioned above, a 5 mm × 5mm large and 46 nm thick Si_3N_4 nanomembrane with a 13 nm Al coating on both sides was found in a previous study[8, 10] to respond to the ion collision with a high frequency vibration caused by thermomechanical forces. Despite the similarity in dimension and composition, the Au-coated Si_3N_4 nanomembrane in our study doesn't vibrate as the Al-coated nanomembrane does. This can be explained by the low thermal expansion coefficient, high flexure rigidity and high density of Au compared with Al. The low thermal expansion of Au, about 60% of that of Al[13], reduces the nanomembrane deformation and thus the strength of thermomechanical force. The flexure rigidity (D) of a material, defined as the resistance offered by a structure undergoing bending, is calculated as

$$D = \frac{Eh^3}{12(1-\sigma^2)} \tag{2}$$

where E is Young's modulus, h is elastic thickness and σ is Poisson ratio. Au has a 20% higher flexure rigidity than Al. Besides, Au is 6 times heavier than Al. Such high density together with the high flexure rigidity substantially damps the effect of the mechanical force that initiates nanomembrane vibration.

3.4 CONCLUSIONS

We obtained the characteristic field emission curves of two types of nanomembranes: one is a 1 mm diameter and 500 nm thick Si_3N_4 nanomembrane with a 15 nm Pt coating on both sides, the other is a 5 mm × 5mm and 30 nm thick Si_3N_4 nanomembrane with a 15 nm Au coating on both sides. Field emission current from the thick nanomembrane was stable and reproducible, while the current from the thin nanomembrane was very unstable and influenced by voltage ramping rate.

Each nanomembrane was then applied to the detection of 9 peptides/proteins in a MALDI-TOF instrument. The thick nanomembrane successfully detected 6 out of 9 samples at a 25 kV acceleration voltage. The unique peak shape in the mass spectra indicates a phonon related enhancement of field emission at ion collision. However, the sensitivity of the detector is low due to the thickness and small active area. Only the two smallest peptides were detected with the thin nanomembrane. The nanomembrane detector response decreases with acceleration voltage (ion kinetic energy) but increases with the electric field strength between the nanomembrane and the grid.

REFERENCES

1. Craighead, H.G. Nanoelectromechanical Systems. *Science*. **290**(5496), 1532-1535 (2000).

2. Ekinci, K.L., Roukes, M.L. Nanoelectromechanical systems. *Rev. Sci. Instrum.* **76**(6), 061101 (2005).

3. Arlett, J.L., Myers, E.B., Roukes, M.L. Comparative advantages of mechanical biosensors. *Nat. Nanotechnol.* **6**(4), 203-215 (2011).

4. Waggoner, P.S., Craighead, H.G. Micro- and nanomechanical sensors for environmental, chemical, and biological detection. *Lab Chip*. **7**(10), 1238-1255 (2007).

5. Calleja, M., Kosaka, P.M., San Paulo, A., Tamayo, J. Challenges for nanomechanical sensors in biological detection. *Nanoscale*. **4**(16), 4925-4938 (2012).

6. Lassagne, B., Garcia-Sanchez, D., Aguasca, A., Bachtold, A. Ultrasensitive Mass Sensing with a Nanotube Electromechanical Resonator. *Nano Lett.* **8**(11), 3735-3738 (2008).

7. Naik, A.K., Hanay, M.S., Hiebert, W.K., Feng, X.L., Roukes, M.L. Towards single-molecule nanomechanical mass spectrometry. *Nat. Nanotechnol.* **4**(7), 445-450 (2009).

8. Park, J., Qin, H., Scalf, M., Hilger, R.T., Westphall, M.S., Smith, L.M., Blick, R.H. A mechanical nanomembrane detector for Time-of-Flight mass spectrometry. *Nano Lett.* **11**(9), 3681-3684 (2011).

9. Fowler, R.H., Nordheim, L. Electron emission in intense electric fields. *Proc. R. Soc. Lond. A*. **119**(781), 173-181 (1928).

10. Park, J., Kim, H., Blick, R.H. Quasi-dynamic mode of nanomembranes for Time-of-Flight mass spectrometry of proteins. *Nanoscale*. **4**(8), 2543-2548 (2012).

11. Park, J., Aksamija, Z., Shin, H.C., Kim, H., Blick, R.H. Phonon-assisted field emission in silicon nanomembranes for Time-of-Flight mass spectrometry of proteins. *Nano Lett.* **13**(6), 2698-2703 (2013).

12. Park, J., Blick, R.H. A silicon nanomembrane detector for matrix-assisted laser desorption/ionization Time-of-Flight mass spectrometry (MALDI-TOF MS) of large proteins. *Sensors*. **13**(10), 13708-13716 (2013).

13. Lide, D.R. Section 12: Properties of Solids, in *CRC Handbook of Chemistry and Physics*, 81st ed. Taylor & Francis: Florida, U.S. (2000).

Table 3.1 Compositions and dimensions of all fabricated nanomembranes

nanomembrane dimension		Si_3N_4 layer thickness (nm)	metal layer			
number of nanomembrane(s)	freestanding region		material	thickness (nm)	front side	back side
16 (4 by 4)	ø 1 mm (each)	500	Pt	15	×	×
4 (2 by 2)	ø 2 mm (each)	500	Pt	15	×	×
1	5 × 5 mm^2	50	Pt	15	×	×
1	5 × 5 mm^2	30	Au	15	×	×
1	5 × 5 mm^2	50	Au	30	×	×
1	5 × 5 mm^2	50	Au	30	×	
1	5 × 5 mm^2	30	Au	30	×	×
1	5 × 5 mm^2	30	Au	30	×	
1	5 × 5 mm^2	50	Al	13	×	×
1	5 × 5 mm^2	30	Al	26	×	×

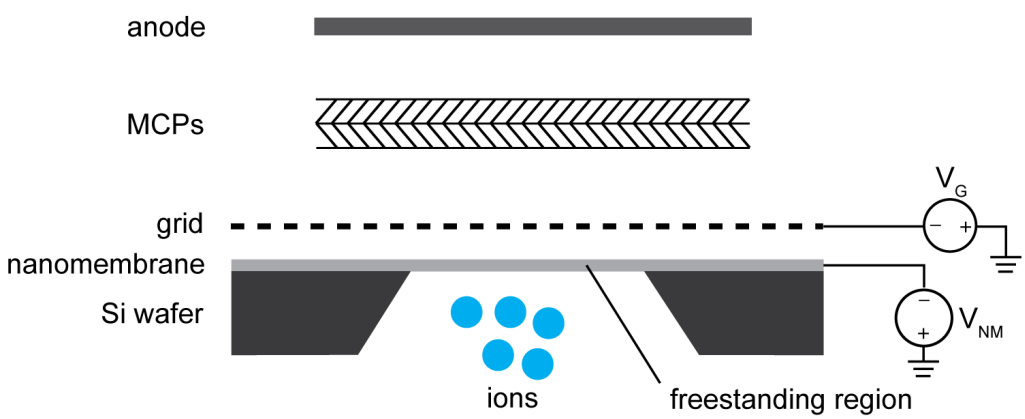

Figure 3.1 Schematic diagram of the nanomembrane detector configuration.

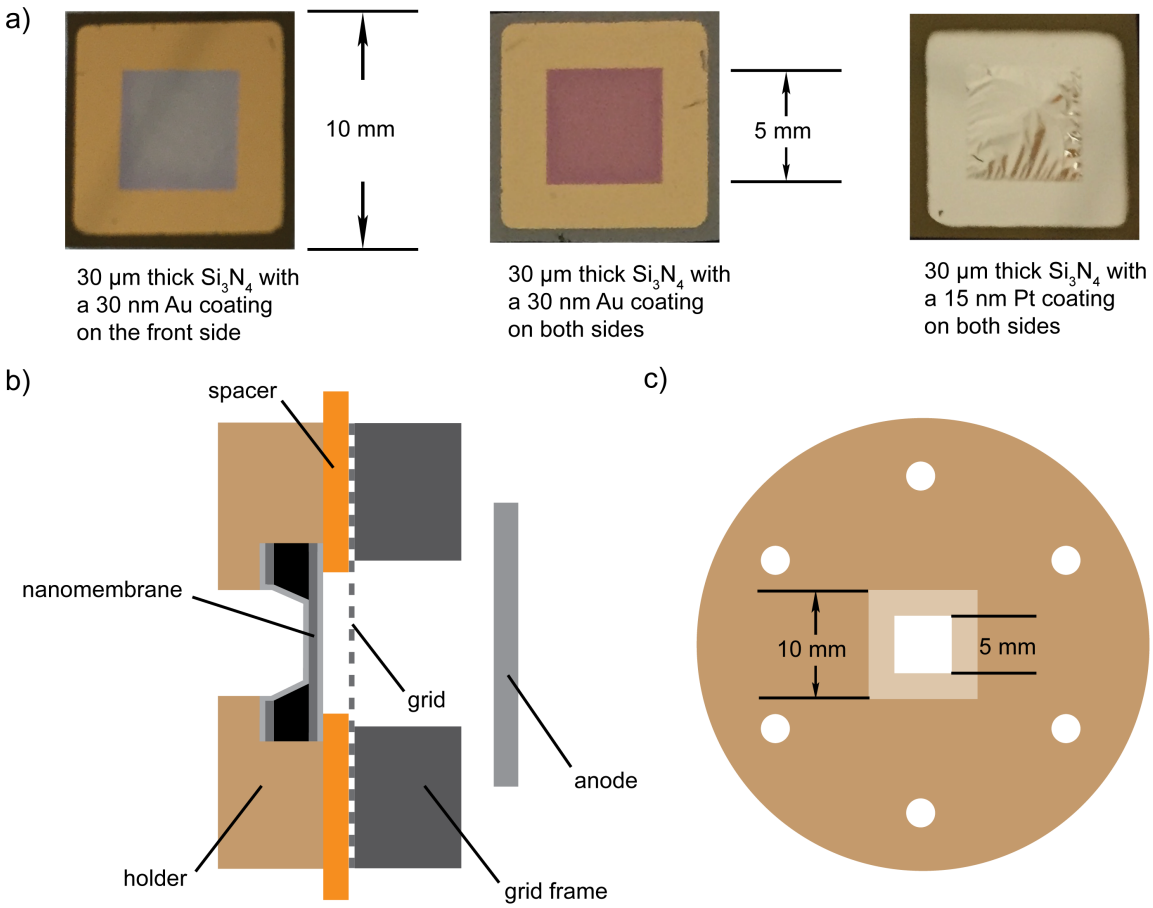

Figure 3.2 a) Pictures of three nanomembranes with their compositions and dimensions specified in the picture. b) Schematic diagram of the device for measuring the field emission current from the nanomembrane. c) Front view of the nanomembrane holder. Dimensions of the central opening and recess are marked.

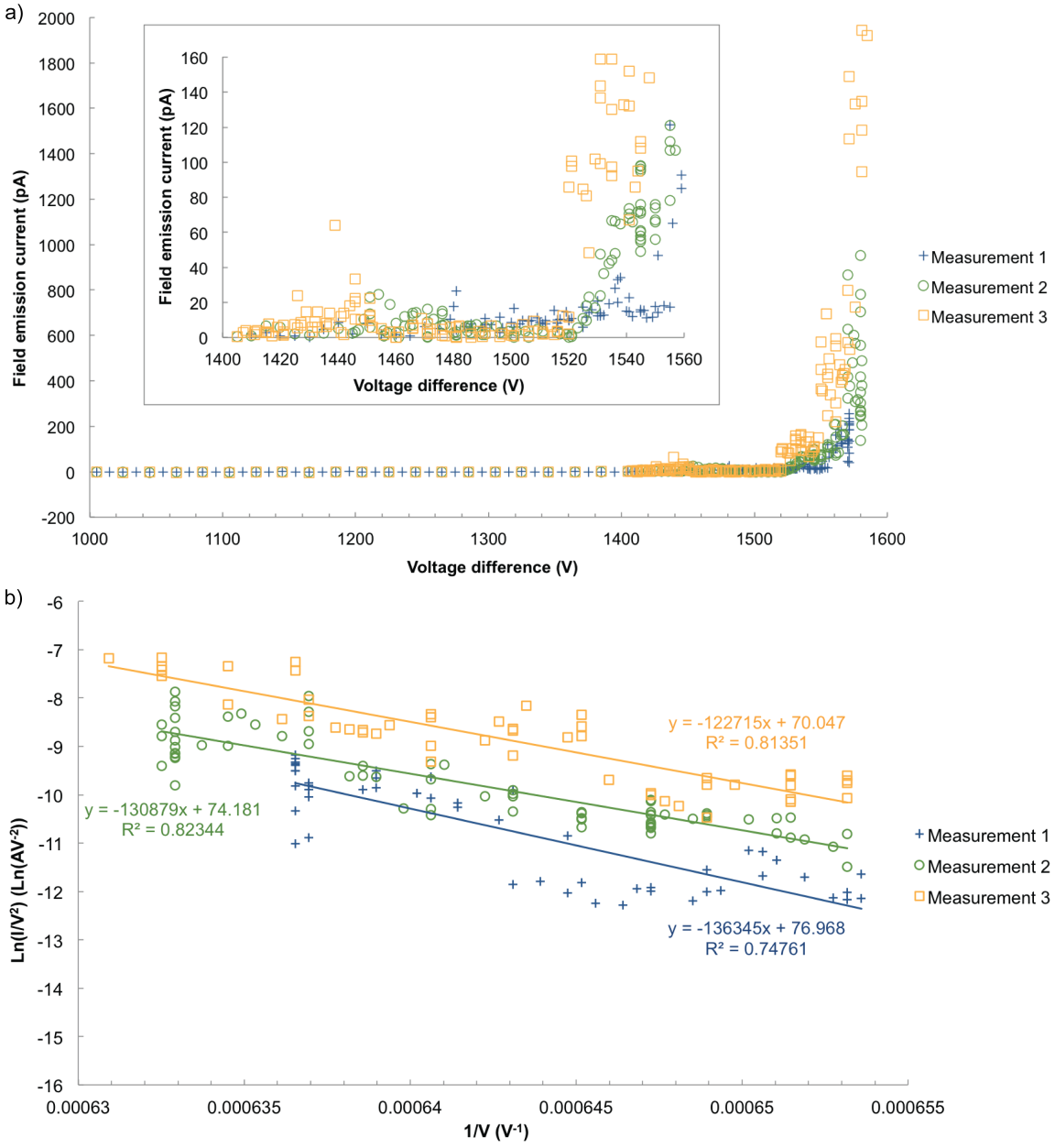

Figure 3.3 a) Field emission I-V curve of a 500 nm thick Pt-coated Si_3N_4 nanomembrane array. The spacer was 0.003" thick and the grid voltage was -300 V. The inset shows the expanded turn-on region. b) Corresponding Fowler-Nordheim plot (only the data points above 1530 V are included). The solid lines are linear fits to the F-N equation.

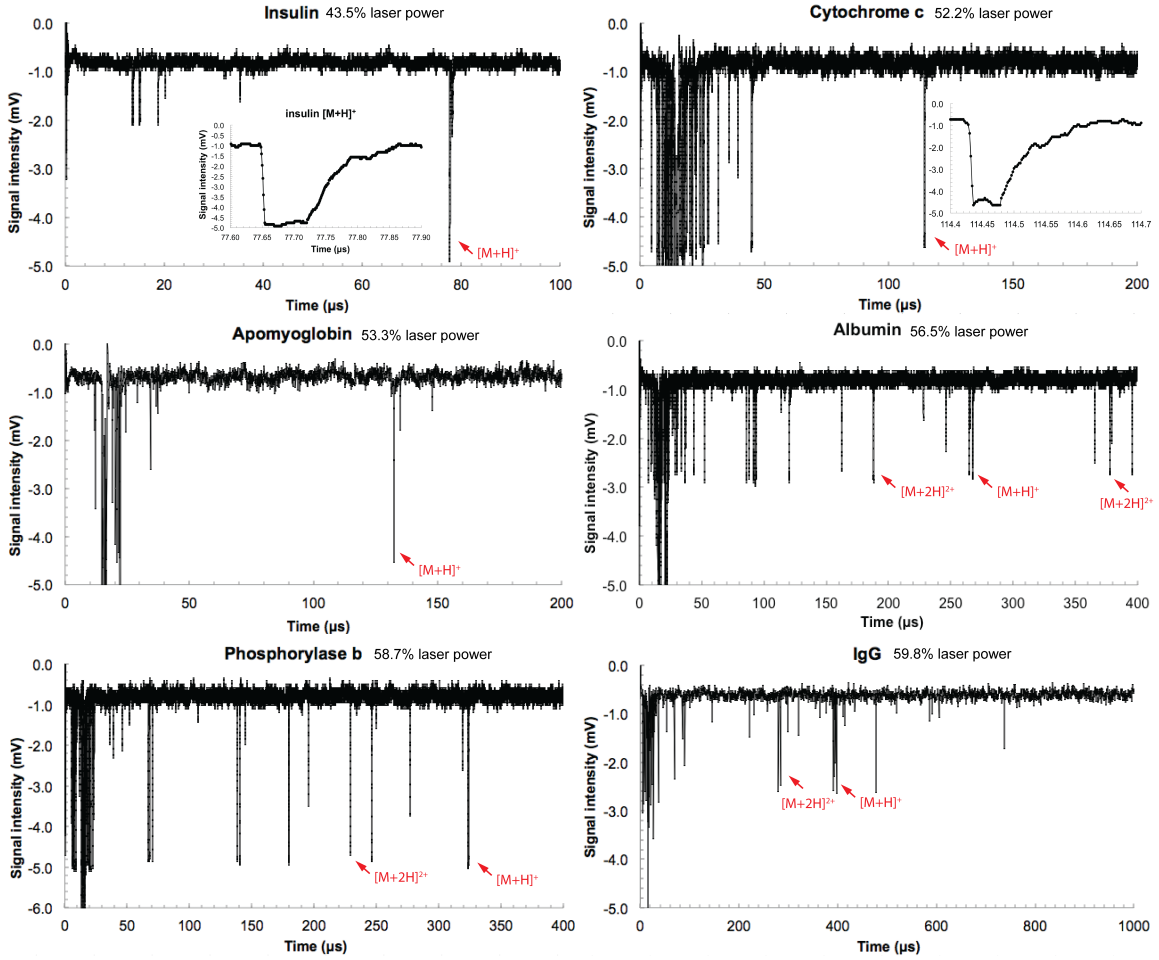

Figure 3.4 Mass spectra of protein samples acquired with the nanomembrane detector incorporating a 500 nm thick Pt-coated Si_3N_4 nanomembrane array at a 25 kV acceleration voltage. Except for the insulin spectrum, the matrix peaks before 40 μs are truncated to expand the protein ion peaks. Laser intensity used for each spectrum is labeled. The identities of the denoted peaks are determined by their masses calculated from the time of flight. The insets in the insulin and cytochrome c spectra are expanded views of the $[M+H]^+$ peaks respectively.

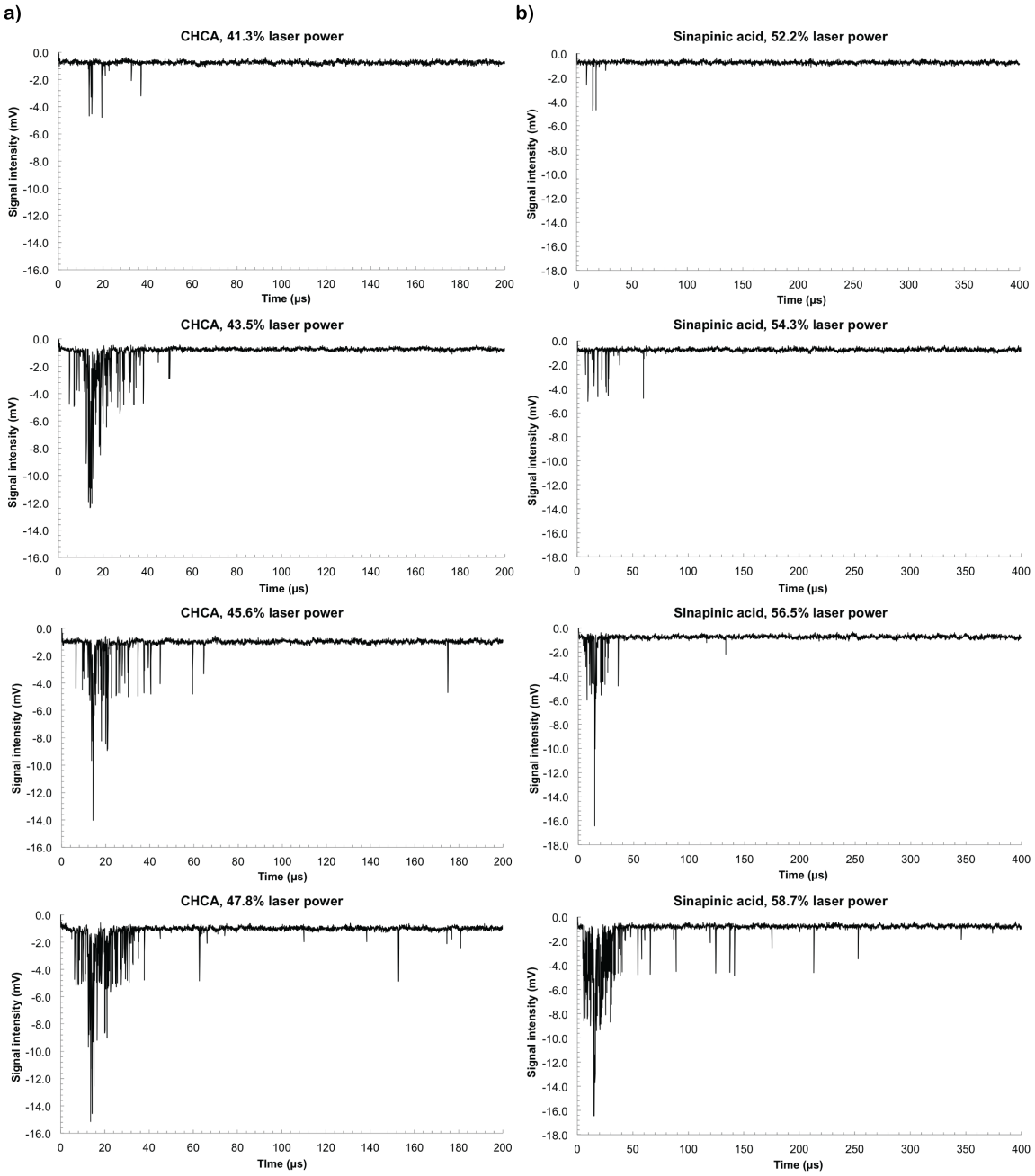

Figure 3.5 Mass spectra of a) CHCA and b) sinapinic acid matrices acquired with the nanomembrane detector incorporating a 500 nm thick Pt-coated Si_3N_4 nanomembrane array at a 25 kV acceleration voltage. Laser intensity used for each spectrum is labeled.

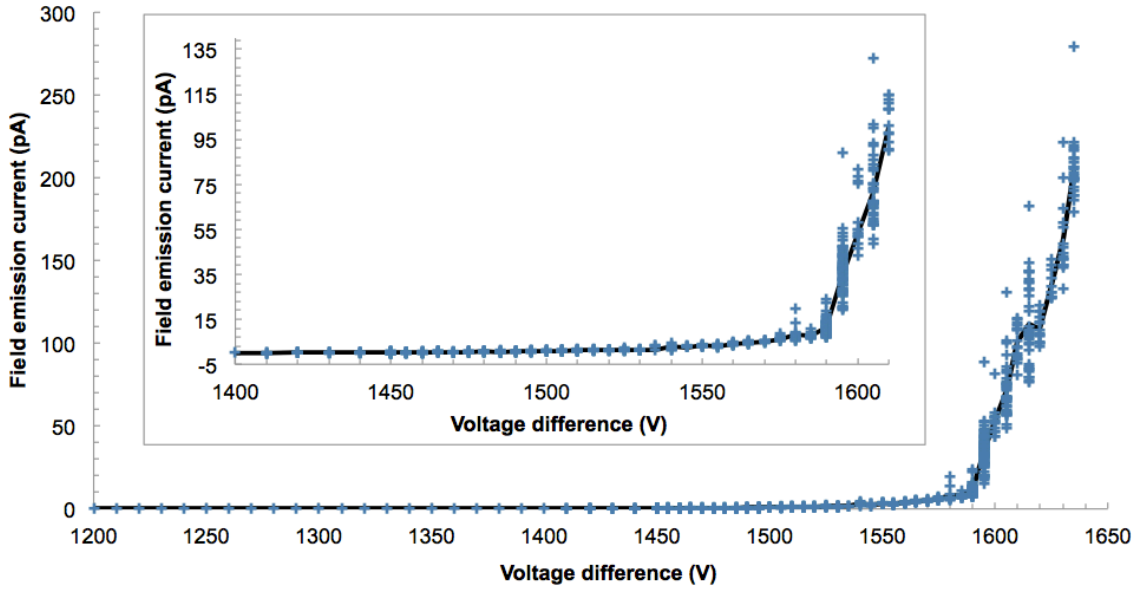

Figure 3.6 Field emission I-V curve of a 30 nm thick Si_3N_4 nanomembrane with a 15 nm Au coating on both sides. The spacer was 0.005" thick and the grid voltage was -300 V. The black curve connects the average current at each voltage difference. The inset shows the expanded turn-on region.

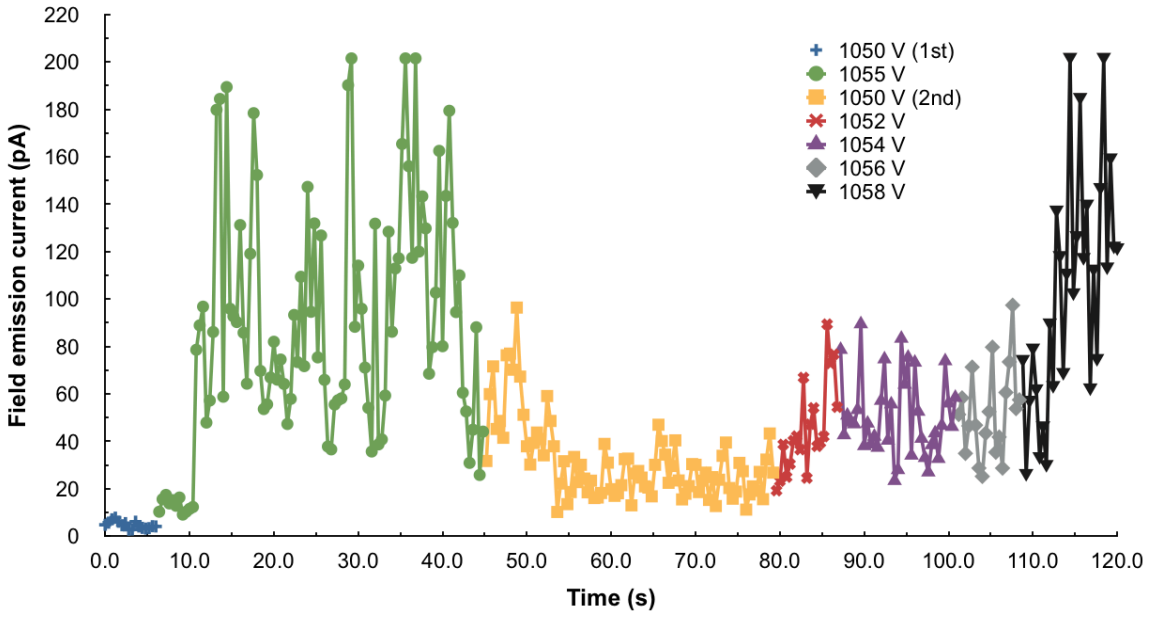

Figure 3.7 Field emission current from a 30 nm thick Si_3N_4 nanomembrane with a 15 nm Au coating on both sides plotted in time sequence. The current readings acquired while the nanomembrane voltage was changing are excluded.

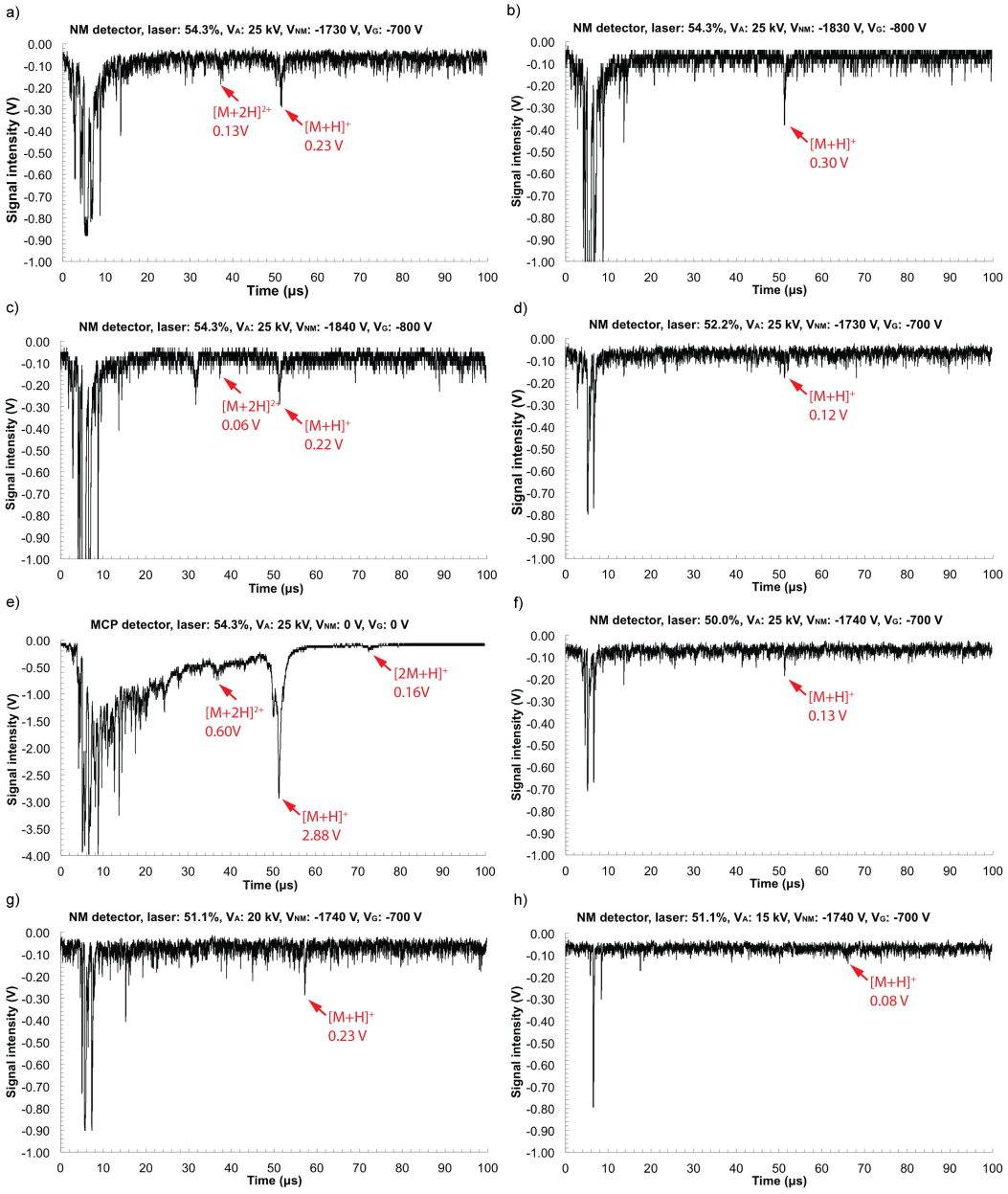

Figure 3.8 ACTH fragment mass spectra acquired with the nanomembrane (NM) detector, incorporating a 30 nm thick Si_3N_4 nanomembrane with a 15 nm Au coating on both sides, under various operation voltages, laser intensities and acceleration voltages (V_A). One spectrum acquired with the MCP detector is shown for comparison. The identified protein peaks and their intensities (after baseline subtraction) are labeled.

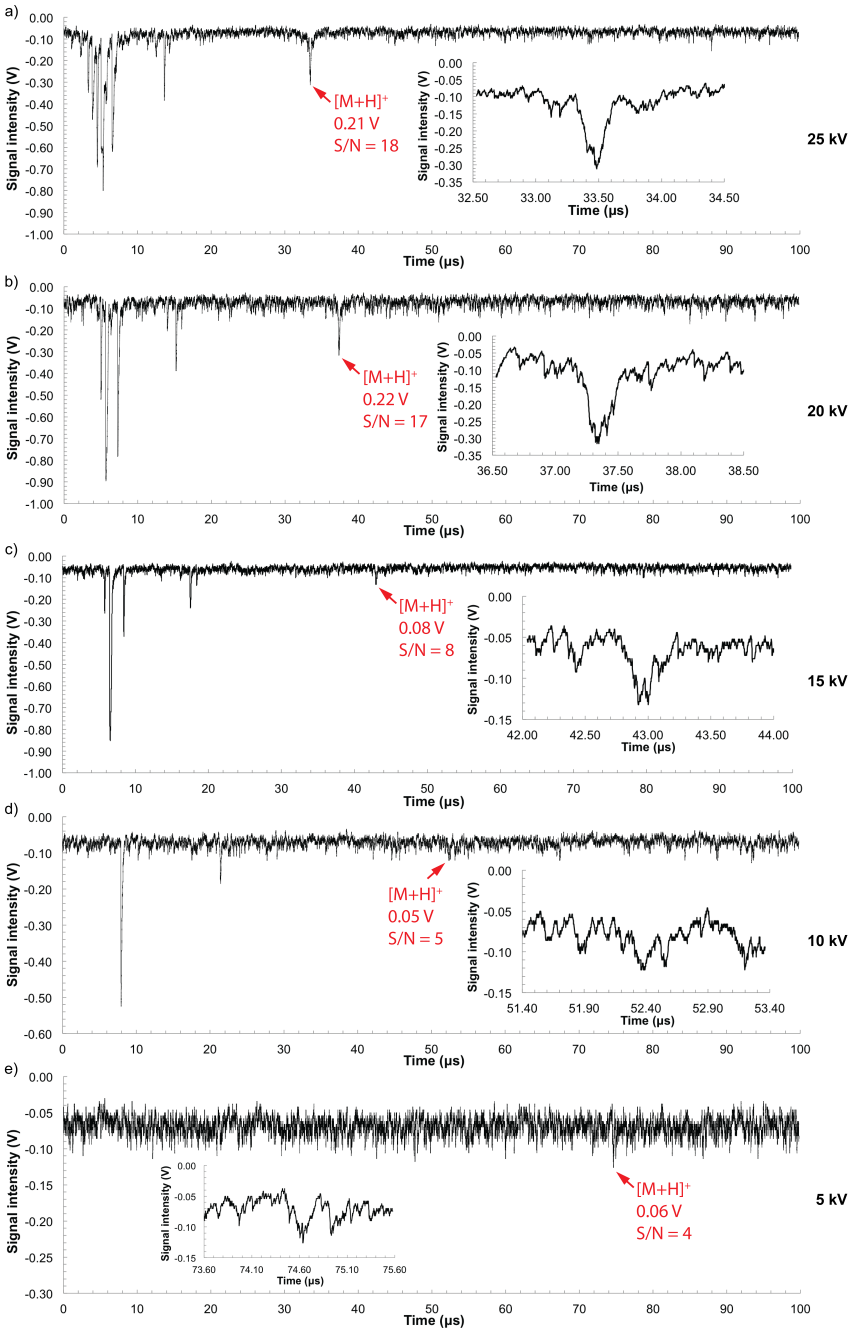

Figure 3.9 Angiotensin II mass spectra acquired at different acceleration voltages with the nanomembrane detector, incorporating a 30 nm thick Si_3N_4 nanomembrane with a 15 nm Au coating on both sides. The identified protein peaks and their intensities (after baseline subtraction) are labeled in the spectra. Insets show the expanded $[M+H]^+$ peaks.

Section 2

CHAPTER 4

Droplet Levitation Integrated with Mass Spectrometry for Single Aerosol Droplet Characterization and Multiphase Reaction Studies

4.1 INTRODUCTION

Atmospheric aerosol particles are liquid droplets or solid particles suspended in air. They influence our climate by absorbing and scattering solar irradiation, forming cloud condensation nuclei and participating in heterogeneous chemical reactions in the atmosphere[1-3]. Aerosol particles also have serious impacts on our health and have been shown to cause disease and cardiovascular damage in high concentrations[4, 5].

A large fraction of fine aerosol mass is made up by organic aerosol (OA). About 20% of the total OA mass is directly emitted from fossil fuel combustion, biomass burning and other sources as primary organic aerosol (POA)[6-9]. The other 80% is from secondary organic aerosol (SOA), which is formed in the atmosphere by partitioning of oxidized gas-phase organic species into the aerosol phase[9, 10]. Both SOA formation and the aging of POA involve multiphase reactions that change the chemical and physical properties of the aerosol particles and thus their effects on the environment. However, those processes are very poorly understood, bringing considerable uncertainties to the prediction of aerosol formation and its impact upon climate simulation[1, 8, 11].

Unlike field measurements, bulk studies and chamber studies are performed under controlled experimental conditions in the laboratory, providing the means to develop mechanistic understanding of atmospheric aerosol formation and growth[12]. Bulk studies are conducted on bulk laboratory samples, which vary significantly from the micron and submicron aerosol droplets in size, surface-to-volume ratio and composition[10, 13]. These studies lack the ability to investigate the effects of multiphase processes and droplet size on chemical composition of the aerosol. In contrast, chamber studies can address both gas-phase chemistry and aerosol dynamics[14, 15]. Since the measurements are made on an ensemble of particles of varying size and composition, the relation between surface-to-volume ratio, interfacial composition and the chemical and physical transformation of the aerosol droplets may be obscure after averaging[16]. In addition, the results are often influenced by wall effects such as removal of gas-phase species and deposition of particles on the wall of the chamber[17, 18].

We are developing a new approach for the online and *in situ* characterization of a single airborne droplet accomplished with droplet levitation techniques. Investigations of multiphase chemical reactions and simultaneous physical property changes of droplets using this system will supplement current studies, bridging the knowledge gap that is otherwise incapable of being directly addressed.

Levitation is critical for conducting experiments on a droplet for extended times, which enables the replication of multiphase reactions in the atmosphere with the gas phase and aqueous phase compositions accurately controlled. Different levitation

techniques have been well developed, including acoustic, optical, electrostatic, aerodynamic, magnetic and superconducting levitation[19]. Among these techniques, only acoustic levitation and optical levitation are suitable for the levitation of micron-sized neutral aerosol droplets.

Acoustic levitation suspends objects by the acoustic radiation force generated from the nonlinear effects of intense sound fields[20, 21]. In a common configuration, samples are levitated at the nodal points of a standing ultrasonic wave created by reflections between an ultrasonic radiator and a reflector[22]. Acoustic levitation has been applied to the study of fluid dynamic[23] and physical properties[24, 25] of liquids in a non-contact manner.

Optical levitation utilizes the radiation pressure of light. The beam waist of a sharply focused Gaussian laser beam by a high numerical aperture objective contains a very strong electromagnetic field gradient, which draws dielectric particles toward the region of highest photon flux, i.e. the center of the beam. The laser beam also applies a scattering force on the particles, pushing it in the direction of beam propagation. When these two forces balance the gravity of the particle, the particle is confined in a three-dimensional trap[26, 27]. This single-beam gradient trap, known as 'optical tweezers', can exert forces exceeding 100 pN[28], which are determined by the steepness of the light gradient and the light intensity[29, 30]. Particles ranging in size from ~20 nm to several micrometers such as DNA molecules[31], organelles[32] and living cells[33, 34] can be stably trapped. Optical tweezers have also been applied to the manipulation of

aerosol particles[16, 35, 36] for studies of coagulation[37], dynamics[38] and heterogeneous reactions[39] in aerosol droplets with Raman spectroscopy.

One of the variants to the Gaussian beam optical tweezers is using a Bessel beam to overcome the rapid diffractive spreading of a Gaussian beam after the focus and achieve an elongated optical trap[40]. A Bessel beam is characterized by a transverse intensity profile of a bright central core surrounded by multiple rings of equal power, which can be described by the zeroth order Bessel function[41]. The ideal Bessel beam requires an infinite amount of energy but a quasi-Bessel beam can be obtained using a conical lens called an axicon. An incident Gaussian beam is refracted by such an optic and the interference of emergent beams results in a Bessel beam core that is non-diffracting and self-healing over a limited spatial range immediately after the axicon[42]. The strong lateral light gradient of the core enables optical trapping but the force is only two-dimensional due to the weak light gradient in the beam propagation direction. The Bessel beam optical tweezers are able to manipulate and guide micron-sized particles in millimeter ranges[42, 43].

Analysis of the chemical compositions of the levitated droplet may be achieved with mass spectrometry, which is highly efficient for sensitive and quantitative detection of ionizable chemical species. A new branch, aerosol mass spectrometry, has been gradually evolving into a powerful tool for aerosol studies in laboratory and field measurements. [44, 45]. Westphall *et al.* demonstrated the possibility of obtaining mass spectra of peptides in a 2-mm diameter acoustically levitated droplet with charge and

matrix-assisted laser desorption/ionization (CALDI)[46]. However, mass spectrometry analysis of an optically trapped droplet hasn't been accomplished so far. The new technique we are developing will combine optical levitation and mass spectrometry, thereby benefiting the study of multiphase chemical reactions in aerosol droplets.

4.2 EXPERIMENTAL

4.2.1 Acoustic levitator

The acoustic levitator was constructed based on the design by Hilger *et al*[47]. It consisted of two homemade pieces, a flat sound emitter and a spherically curved reflector as illustrated by Figure 4.1. The emitter was a 31.8 mm-diameter thin aluminum disk that was vibrating at 20 kHz driven by an acoustic transducer (Misonix, Farmingdale, NY). The aluminum reflector had a section radius of 21.6 mm and a curvature radius of 33.5 mm. The distance between the emitter and the reflector was precisely adjusted to produce a standing sound wave in the middle. Two nodes existed in the standing wave but the upper one was more accessible and thus used for droplet levitation. The emitter and the reflector were enclosed in a chamber made of thin Mylar film. The humidity around the levitated droplet was regulated by tuning the flow rate of humidified air into the chamber. A droplet was initially formed and introduced into the trap at the tip of a syringe or a capillary. After the syringe or capillary was retracted quickly by a solenoid, the droplet was left trapped. The levitated droplet was observed through a TM-200 CCD camera (JAI Pulnix, Sunnyvale, CA).

4.2.2 Gaussian beam optical tweezers

The Gaussian beam optical tweezers shown in Figure 4.2 were built based on the schematic provided by Smith *et al*[48]. A Ventus 532 nm continuous wave laser (Laser Quantum, Cheshire, UK) with tunable power up to 750 mW was used. The laser beam was directed into a telescope composed of lens L1 (f = 19 mm) and L2 (f = 50 mm) by mirror M1 and M2 and expanded into a collimated beam, which was then converted by L3 (f = 175 mm) into a beam with the appropriate size and curvature at the back of a 60x microscope objective (Nikon PlanApo 60, numerical aperture = 1.40 (oil), working distance = 0.17 mm. Nikon, Belmont, CA). The beam was steered by M3 and M4 onto a 532 nm dichroic mirror (Chroma Technology, Bellows Falls, VT), which reflected the incoming laser beam straight into the objective but allowed the transmission of illumination light coming out of the objective. An image was formed at the focal plane of L4 (f = 50 mm) and captured by a TM-200 CCD camera. A 590 nm longpass colored glass filter was inserted in front of the camera to remove any transmitted laser beam by the dichroic mirror. All optical components employed here were obtained from Thorlabs (Newton, NJ) if not otherwise specified.

The optical tweezers were first tested on trapping 3 μm-diameter polystyrene beads dispersed in water (Sigma-Aldrich, St. Louis, MO). The sample was prepared by placing 20 μL of the diluted beads solution on a microscope slide and covered by a No.1 coverslip (0.13 to 0.17 mm thick). The sample slide was mounted on a XYZ translational stage upside down so that the coverslip was touching the thin layer of immersion oil on

the objective. The vertical position of the sample slide was precisely adjusted to enclose the laser beam focus within the sample solution, merely 10 μm thick.

Aerosol droplets were generated from a solution containing 10 mM $(NH_4)_2SO_4$ with a ultrasonic nebulizer (Mabis, Waukegan, IL). $(NH_4)_2SO_4$ was added to decrease the vapor pressure of the droplets. The droplets were blown into a 2000 cm^3 large chamber made of thin Mylar film from an opening at the top. At the bottom of the chamber, a 2.5 cm-diameter hole was opened in the film as the orifice with the objective. The hole was covered by a piece of 35 mm × 50 mm coverslip (Fisher Scientific, Pittsburgh, PA) that was in contact with the objective via immersion oil.

4.2.3 Bessel beam optical tweezers

The schematic diagram of the Bessel beam optical tweezers is shown in Figure 4.3, which is based on the one built by Meresman *et al*[43]. The Ventus 532 nm laser was operated at the maximum power of 750 mW. The Gaussian beam was converted to a Bessel beam after passing through an axicon that has an apex angle of 170° (Edmund optics, Barrington, NJ). The Bessel beam was reduced by 8 times with a beam reducer consisted of two plano-convex lenses, L1 (f = 200 mm) and L2 (f = 25.4 mm) (Thorlabs, Newton, NJ). The optical tweezers formed at the focus of L2 and were protected by a house-made Teflon chamber. The Teflon chamber was 8.8 cm tall and the interior was 1.0 cm × 1.5 cm wide. Two microscope slides were embedded on two opposite sides of the chamber serving as windows.

Aerosol droplets were generated by a medical nebulizer (Omron, Lake Forest, IL) and introduced into the chamber through a Y connector on the chamber lid. A pinch valve was used to shut off the aerosol flow before excessive amount of droplets went into the chamber. A coverslip was placed about 0.5 cm from the bottom of the chamber to prevent contamination of L2. High concentration of NaCl was added to the nebulizing solution to reduce the vapor pressure of the droplets.

The upward radiation pressure of the high power laser beam exerted on the trapped droplet was greater than the droplet gravity. We utilized the Stokes' drag from a downward laminar flow of N_2 to counteract the net force. N_2 was introduced into the chamber from the other branch of the Y connector after flowing through a water bubbler. The interior of the chamber lid was streamlined to facilitate the formation of the laminar flow. The humidity in the vicinity of the trap was regulated by the amount of water vapor carried in the N_2 flow, which was realized by heating the water with heat tapes. The flow rate was controlled with a mass flow controller (Alicat Scientific, Tucson, AZ) for the purpose of precisely adjusting the vertical position of the levitated droplet. The stability of the trap was greatly improved by diffusing the N_2 through a gas dispersion tube at the inlet of the water bubbler.

A long working distance objective (Olympus LMPLFLN 10x, numerical aperture = 0.25, working distance = 21 mm. Olympus, Center Valley, PA) was used to collect the scattered laser light from the levitated droplet at 90° to the incident beam through the glass window. The scattered light was further expanded by a TM-200 CCD camera

equipped with an 8x zoom lens (Edmund optics, Barrington, NJ), resulting in a total magnification of 2400x that permitted the observation of bright-field images of the droplet as well. A 570 nm longpass colored glass filter was placed in front of the camera to reduce the scattered light intensity. The image obtained on the CCD camera was recorded on a computer via a video converter (Kworld, Brea, CA) and processed by the software PowerDirector v. 10 (CyberLink, Santa Clara, CA).

4.2.4 Bessel beam optical tweezers integrated with Electrospray ionization (ESI)-MS

The Teflon chamber was modified to interface with the homemade ESI source and the Bruker MicrOTOF mass spectrometer (Billerica, MA) as depicted in Figure 4.4. A 5 mm-thick and 1.5 cm-wide Teflon piece was carved out from the interior surface of the chamber wall against the mass spectrometer and screwed to the lid, which was connected to a solenoid. The Teflon piece blocked a 0.64 cm-diameter aperture on the wall. A homemade stainless steel nozzle was tightly inserted into the aperture as extended mass spectrometer inlet. The vacuum inside the mass spectrometer drew the Teflon piece against the chamber and an O-ring was embedded in the wall for a better seal.

On the opposite side of the chamber, a tapered stainless steel emitter (New Objective, Woburn, MA) with a 50 μm inner diameter and 320 μm outer diameter was inserted into the chamber. The emitter was coaxial with the nozzle and very close to the levitated droplet. The droplet was levitated for 1 to 3 hours until all the other droplets in the background were no longer observable. The emitter was retracted to prevent

contamination during this process. Electrospray solution consisting of 50/50 Methanol/H_2O with 0.1% formic acid was pumped into the emitter by a syringe at 10 μL/h. When the levitated droplet was ready for mass spectrometry analysis, a tiny drop of electrospray solution was allowed to form at the tip of the emitter. Then a high voltage of 4230 V was applied to the emitter and a highly charged liquid jet was fired to the droplet. The Teflon piece was lifted up together with the lid by the solenoid at the same time or immediately after the voltage was applied. Attempts were made on this apparatus to acquire mass spectra of levitated droplets containing hexylammonium chloride, histidine or CsCl.

4.3 RESULTS AND DISCUSSION

4.3.1 Acoustic levitation of aqueous droplets

The acoustic levitator is highly efficient at trapping droplets from 0.4 to 1.5 mm in diameter and the droplet can remain in the trap for more than 4 hours. A picture of an acoustically levitated droplet is shown in Figure 4.5. The trapping force applied to the droplet is so strong that sometimes the droplet is squeezed into an egg shape. Most of the time the levitated droplet does not stay still in one spot but vibrates and oscillates in a sinusoidal manner. The oscillation becomes more vigorous as the droplet gets smaller. Under a diameter of 80 μm, the droplet is no longer traceable by the camera. The vibration and shape oscillation of acoustically levitated droplets have been explored by theoretical and experimental studies in previous publications[20, 49, 50]. The oscillations

of the droplet are a result of the varying restoring force, i.e. the summation of acoustic radiation force and gravity, which is approximately proportional to the distance from equilibrium point. The vibration frequency increases as the volume of the droplet decreases.

The droplet grows and shrinks with the regulated humidity change inside the chamber, which provides an advanced platform for the study of how wetting and drying influence the organic compounds in aerosol droplets and cloud droplets. However, the steadily levitated droplet is at least 20 times larger than a typical cloud droplet and more than 400 times larger than an aerosol droplet. This significant difference in size and surface-to-volume ratio could bring differences to the chemistry of the droplet. For example, when the reaction involves gas-phase species, the surface-to-volume ratio of the droplet is crucial to the reaction rate. In order to levitate micron droplets that are more close to aerosol droplets we wish to study, optical tweezers were explored as an alternative levitation method.

4.3.2 Aqueous droplet levitation with Gaussian beam optical tweezers

Three–micron polystyrene beads in aqueous solution make excellent test objects for aligning the optical tweezers due to their relatively high refractive index in comparison with water that can increase the light gradient in the beam focus. When the beads float within ~10 μm from the optical tweezers at a speed below ~40 μm/s, they will suddenly deviate from the original path and fall or rise into the trap. The beads cease any

movement and stay in the trap even when the sample slide is translated laterally or vertically. Figure 4.6 is a picture of three trapped polystyrene beads. About 20 beads can be confined in the optical tweezers simultaneously and form a close-packed layer of beads at merely 10 mW laser power, measured at the back aperture of the objective. Further turning up the laser power causes the sample solution to dry out faster without significantly improving the trapping efficiency.

The optical tweezers were applied to the capture of nebulized aqueous droplets floating in the chamber. The optical tweezers are able to occasionally catch a droplet that is flying through the trap at a very low speed, while most droplets eventually crash into the chamber wall and the coverslip. To capture a 10 μm-diameter droplet, a minimum power of 60 mW is required at the back aperture of the objective. The trapped droplet vibrates and tends to escape with the help of nearby air turbulence. The low viscosity of air can only damp the Brownian motion of the trapped droplet[51] so lightly that the droplet may still possess enough kinetic energy to escape. In contrast, the liquid water assists the trapping of polystyrene beads by strongly damping their Brownian motion.

The objective used to focus the laser beam has a working distance of 0.17 mm, meaning the levitated droplet is about 170 μm above the objective lens, but there is immersion oil and a coverslip in this space also. Therefore, the space between the levitated droplet and the coverslip is no more than 40 μm (coverslip thickness ≥ 130μm). Given this short distance, the majority of the droplets that are close to the trap fall onto the coverslip. Since the trapping efficiency depends highly on the frequency of a slow

droplet getting very close to the trap, this current setup does not provide effective capturing of airborne droplets.

The extremely short working distance of the objective also brings difficulties to the ionization of the droplet when coupling with mass spectrometry. The weak trapping force is incapable of holding the droplet in place during ionization so the droplet is very likely to fall onto the coverslip. In addition, droplets fallen on the coverslip are ionized at the same time, bringing about high background signals. Efforts have been made to replace the objective with a simple lens (f = 25 mm), but the light gradient of the laser beam focused by a simple lens was too low to capture even a polystyrene bead, even when the highest laser power was used.

4.3.3 Aqueous droplet levitation with Bessel beam optical tweezers

The intrinsic light gradient in the Bessel beam core is comparable to a Gaussian beam focused by a high numerical aperture objective. The strength of the Bessel beam optical tweezers relies heavily on the Bessel beam quality. The Bessel beam profile is mainly determined by the shape of the axicon and is influenced by the incident Gaussian beam profile and incident angle. No axicon is perfectly conical. Common manufacturing defects include rounded tips and elliptical cross sections. We evaluated three axicons with different apex angles from two manufacturers and only one generated a high quality Bessel beam. The cross-sectional profile of the Bessel beam at the focus of lens 2 is shown in Figure 4.7a.

The Bessel beam intensity profile can be expressed by[52]

$$I(r,z) = \frac{4k_r P}{w} \frac{z}{z_{\max}} J_0^2(k_r r) \exp(-\frac{2z^2}{z_{\max}^2}) \quad (1)$$

where J_0 is the zeroth-order Bessel function of the first kind, r is the radial displacement, z is the displacement along the direction of propagation, P and w are the power and beam waist of the incident beam respectively. k_r=$k$sinα, where k is the angular wavenumber of the incident beam. α is calculated from the opening angle of the axicon γ by

$$\alpha = \arcsin(n \sin\gamma) - \gamma \quad (2)$$

where n is the refractive index of the axicon. $z_{\max}$ is the propagation distance of the Bessel beam in which interference occurs

$$z_{\max} = w(\cot\alpha - \tan\gamma) \quad (3)$$

Figure 4.7b is a simulated intensity profile of the Bessel beam generated in the experiment based on equation (1). The Bessel beam core is theoretically 4.8 mm long and 1.4 μm in diameter and the brightest region of the core is 1.1 mm away from its origin. The maximum laser intensity in the core is less than 25 mW after being absorbed and reflected by the optics along the path. The Bessel beam core length is measured to be about 6 mm, which is a little longer than the theoretical value. We believe the actual diameter of the core is slightly larger than 1.4 μm as well.

The force exerted on the droplet in the Bessel beam core can be divided into a radial trapping force that draws the droplet towards the beam center and a upward

propelling force, both of which are proportional to the laser intensity. In our case, when the trapping force confines a droplet in the trap, the propelling force is much stronger than the gravitational force (G) on the droplet. We observe that the droplet shoots up straight along the core and finally disappears at the end of the Bessel beam. We utilize the Stokes' drag (F_d) from a laminar N_2 flow to counteract the propelling force (F_p). The droplet will stop rising when reaching an equilibrium at $F_p = F_d + G$. This dynamic equilibrium can only occur from the intensity maximum to the end of the Bessel beam core. In this particular region, when the droplet is displaced from the equilibrium position, for example, slightly upward, the propelling force becomes weaker because of the decreased beam intensity and a net downward force restores the droplet to the equilibrium position. For a 4 um-diameter droplet (gravitational force = 0.5 pN), the Stokes' drag from the N_2 flow at 10 cm/min is approximately 1.1 pN and therefore the propelling force is about 1.6 pN.

The Bessel beam optical tweezers are very reliable. The efficiency of capturing one droplet from the nebulized mist is almost 100% and the equilibrium position is reproducible at constant N_2 flow rate. Since the Bessel beam core is non-diffracting and self-healing in a limited range, multiple droplets can be trapped at the same time in different locations along the core. However, only the droplets with an optimal size can last more than one hour in the trap. Heavier droplets gradually descend and lighter ones eventually dry up. We are able to levitate a 4-μm diameter droplet for more than 3 hours and move it steadily up and down within a 3-mm range by adjusting the Stokes' drag via

the N_2 flow rate. The vertical translation of the droplet can also be achieved by moving lens 2.

Figure 4.8 is a picture of a levitated droplet in the Bessel beam optical tweezers. The levitated droplet can be directly observed by human eyes through its light scattering. Magnifying the scattered light enables us to scrutinize the behavior of the droplet in the trap. The instability of the N_2 flow into the water bubbler causes a high-frequency vertical oscillation of the droplet in a 10-μm range. So the scattered light pattern can only be clearly distinguished when the camera's shutter is set at a high speed. The pattern varies with the droplet diameter, composition and location in the beam. Two scattering patterns are shown in Figure 4.9a as examples. A sudden relocation of the droplet to another equilibrium position is often accompanied by a change in its scattering light pattern, suggesting growth or shrinkage of the droplet. In general, the levitated droplet is very stable in the trap, but a rare and interesting partition-and-reunion process of a droplet has been recorded (snapshots shown in Figure 4.9b). The droplet suddenly splits into two droplets, both of which are still trapped about 10 μm apart. After dwelling in their own equilibrium positions for about a minute, they collide with each other and merge into one droplet again.

4.3.4 Analysis of the levitated droplet in a Bessel beam optical tweezers with ESI-MS

Mass spectra of levitated droplets containing hexylammonium chloride, histidine or CsCl were obtained. The extracted ion chromatogram of Cs^+ ions in a levitated droplet

is shown in Figure 4.10. The droplet was generated from a solution containing 6 M NaCl and 0.3 M CsCl. The signal of Cs^+ ions shows up immediately after the start of electrospray (0.0 s in the mass chromatogram), and then quickly drops back to zero. Due to the inherent fluctuation of electrospray, the intensity of Cs^+ ion peak is normalized to the intensity of the most abundant background peak in the spectrum. The spike at 3.4 s in the chromatogram is probably caused by Cs^+ ions from another droplet, suggesting the free droplets nebulized into the chamber were not completely removed before the start of analysis. This is supported by the fact that similar results were also obtained in some of the control experiments when no droplet was trapped. Under the current experimental conditions, the chamber is flushed with fresh N_2 gas every 45 s for 1 to 3 hours. The N_2 flow carries nearly all the other droplets out of the chamber, but a few may linger at the bottom where the N_2 gas flow is reflected by the coverslip.

Another source of the background signal comes from the gas-phase analyte molecules evaporated from the thousands of nebulized droplets. In the case of Cs^+, the contribution of gas-phase analyte is negligible since Cs^+ ion has a very low volatility, so the baseline of the extracted ion chromatogram stays at zero as shown in Figure 4.10. However, when the analyte is switched from CsCl to hexylammonium chloride, a constant signal of hexylammonium is observed by the mass spectrometer due to the high vapor pressure of hexylamine. Similarly, the extracted ion chromatogram obtained for the histidine-containing droplet also has a low background.

A solution to the background interference would be to generate and introduce a

single droplet directly into the trap. In addition to being precisely delivered to the trapping location, the droplet needs to be a proper size and have an appropriate speed to allow it to be trapped. A droplet generator satisfying the above requirements is under construction.

The experimental apparatus also suffers from poor reproducibility. Analyte ion signal appears only in a small fraction of the measurements, which is attributed to the low ionization efficiency of the ESI system. Ionization of the analyte molecules involves interaction of the droplet with the highly charged electrospray droplets for charge transfer as well as desolvation of the droplet. The ionization efficiency depends on the completeness of these two processes before the droplet is drawn into the mass spectrometer in less than a second. It's highly possible that the levitated droplet can't acquire enough charges from the electrospray droplets during such a short time. Other ionization methods have been evaluated and corona discharge was selected as an alternative to ESI. Corona discharge is the heart of atmospheric pressure chemical ionization (APCI). Ionization of the analyte occurs by reacting with the ionized gas molecules surrounding a corona discharge electrode. Our group has successfully applied a negative corona to the charge reduction of electrospray-generated protein ions[53]. We used the same device to ionize molecules in positive mode. The corona discharge ionization source is a short nozzle mounted on the mass spectrometer inlet. Corona discharge takes place in a branch of the nozzle filled with humidified N_2 and generates numerous positive ions such as positively charged water molecules. The merit of this

design is that the droplet continuously interacts with those positive ions when traveling through the nozzle. The corona discharge ionization source exhibits exceptional efficiency and stability in preliminary experiments. The downside of its high sensitivity is that a high background is observed. The mass spectra of air and N_2 show numerous intense peaks spread over a wide mass range. The removal of these background species in the air and N_2 surrounding the Bessel beam optical tweezers is under investigation.

4.4 CONCLUSIONS

Three droplet levitation devices were built and investigated for the goal of studying chemistry in a levitated aerosol droplet with mass spectrometry. The acoustic levitator is less complicated and more powerful than the two types of optical tweezers. Stable levitation of an aqueous droplet at a diameter of hundreds of microns was achieved with the acoustic levitator. The Gaussian beam optical tweezers built with a high numerical aperture objective was able to trap a 10 μm-diameter droplet. However, the short distance between the levitated droplet and the objective is an obstacle to mass spectrometric analysis of the droplet. The Bessel beam optical tweezers enabled ESI-MS analysis of a 4 μm-diameter trapped droplet. Further improvements to the current setup are necessary to increase the ionization efficiency of the analyte molecules as well as to reduce the interference from the analyte in other droplets.

REFERENCES

1. Hallquist, M., Wenger, J.C., Baltensperger, U., Rudich, Y., Simpson, D., Claeys, M., Dommen, J., Donahue, N.M., George, C., Goldstein, A.H., Hamilton, J.F., Herrmann, H., Hoffmann, T., Iinuma, Y., Jang, M., Jenkin, M.E., Jimenez, J.L., Kiendler-Scharr, A., Maenhaut, W., McFiggans, G., Mentel, T.F., Monod, A., Prévôt, A.S.H., Seinfeld, J.H., Surratt, J.D., Szmigielski, R., Wildt, J. The formation, properties and impact of secondary organic aerosol: current and emerging issues. *Atmos. Chem. Phys.* **9**(14), 5155-5236 (2009).

2. Horstmann, M., Probst, K., Fallnich, C. Towards an integrated optical single aerosol particle lab. *Lab Chip*. **12**(2), 295-301 (2012).

3. Mitchem, L., Reid, J.P. Optical manipulation and characterisation of aerosol particles using a single-beam gradient force optical trap. *Chem. Soc. Rev.* **37**(4), 756-769 (2008).

4. Dickery, D.W., Pope, C.A. Acute respiratory effects of particulate air pollution. *Annu. Rev. Public Health*. **15**, 107-132 (1994).

5. Geiser, M., Rothen-Rutishauser, B., Kapp, N., Schürch, S., Kreyling, W., Schulz, H., Semmler, M., Hof, V.I., Heyder, J., Gehr, P. Ultrafine Particles Cross Cellular Membranes by Nonphagocytic Mechanisms in Lungs and in Cultured Cells. *Environ. Health Persp.* **113**(11), 1555-1560 (2005).

6. Spracklen, D.V., Jimenez, J.L., Carslaw, K.S., Worsnop, D.R., Evans, M.J., Mann, G.W., Zhang, Q., Canagaratna, M.R., Allan, J., Coe, H., McFiggans, G., Rap, A., Forster, P. Aerosol mass spectrometer constraint on the global secondary organic aerosol budget. *Atmos. Chem. Phys.* **11**(23), 12109-12136 (2011).

7. Zhang, Q., Jimenez, J.L., Canagaratna, M.R., Allan, J.D., Coe, H., Ulbrich, I., Alfarra, M.R., Takami, A., Middlebrook, A.M., Sun, Y.L., Dzepina, K., Dunlea, E., Docherty, K., DeCarlo, P.F., Salcedo, D., Onasch, T., Jayne, J.T., Miyoshi, T., Shimono, A., Hatakeyama, S., Takegawa, N., Kondo, Y., Schneider, J., Drewnick, F., Borrmann, S., Weimer, S., Demerjian, K., Williams, P., Bower, K., Bahreini, R., Cottrell, L., Griffin, R.J., Rautiainen, J., Sun, J.Y., Zhang, Y.M., Worsnop, D.R. Ubiquity and dominance of oxygenated species in organic aerosols in anthropogenically-influenced Northern Hemisphere midlatitudes. *Geophys. Res. Lett.* **34**(13), L13801 (2007).

8. Jimenez, J.L., Canagaratna, M.R., Donahue, N.M., Prevot, A.S., Zhang, Q., Kroll, J.H., DeCarlo, P.F., Allan, J.D., Coe, H., Ng, N.L., Aiken, A.C., Docherty, K.S., Ulbrich, I.M., Grieshop, A.P., Robinson, A.L., Duplissy, J., Smith, J.D., Wilson,

K.R., Lanz, V.A., Hueglin, C., Sun, Y.L., Tian, J., Laaksonen, A., Raatikainen, T., Rautiainen, J., Vaattovaara, P., Ehn, M., Kulmala, M., Tomlinson, J.M., Collins, D.R., Cubison, M.J., Dunlea, E.J., Huffman, J.A., Onasch, T.B., Alfarra, M.R., Williams, P.I., Bower, K., Kondo, Y., Schneider, J., Drewnick, F., Borrmann, S., Weimer, S., Demerjian, K., Salcedo, D., Cottrell, L., Griffin, R., Takami, A., Miyoshi, T., Hatakeyama, S., Shimono, A., Sun, J.Y., Zhang, Y.M., Dzepina, K., Kimmel, J.R., Sueper, D., Jayne, J.T., Herndon, S.C., Trimborn, A.M., Williams, L.R., Wood, E.C., Middlebrook, A.M., Kolb, C.E., Baltensperger, U., Worsnop, D.R. Evolution of organic aerosols in the atmosphere. *Science*. **326**(5959), 1525-1529 (2009).

9. Kanakidou, M., Seinfeld, J.H., Pandis, S.N., Barnes, I., Dentener, F.J., Facchini, M.C., Van Dingenen, R., Ervens, B., Nenes, A., Nielsen, C.J., Swietlicki, E., Putaud, J.P., Balkanski, Y., Fuzzi, S., Horth, J., Moortgat, G.K., Winterhalter, R., Myhre, C.E.L., Tsigaridis, K., Vignati, E., Stephanou, E.G., Wilson, J. Organic aerosol and global climate modelling: a review. *Atmos. Chem. Phys.* **5**(4), 1053-1123 (2005).

10. Blando, J.D., Turpin, B.J. Secondary organic aerosol formation in cloud and fog droplets: a literature evaluation of plausibility. *Atmos. Environ.* **34**(10), 1623-1632 (2000).

11. Nah, T., Chan, M., Leone, S.R., Wilson, K.R. Real time in situ chemical characterization of submicrometer organic particles using direct analysis in real time-mass spectrometry. *Anal. Chem.* **85**(4), 2087-2095 (2013).

12. Cocker, D.R., Flagan, R.C., Seinfeld, J.H. State-of-the-Art Chamber Facility for Studying Atmospheric Aerosol Chemistry. *Environ. Sci. Technol.* **35**(12), 2594-2601 (2001).

13. Altieri, K.E., Carlton, A.G., Lim, H.-J., Turpin, B.J., Seitzinger, S.P. Evidence for Oligomer Formation in Clouds: Reactions of Isoprene Oxidation Products. *Environ. Sci. Technol.* **40**(16), 4956-4960 (2006).

14. Haan, D.O.D., Corrigan, A.L., Smith, K.W., Stroik, D.R., Turley, J.J., Lee, F.E., Tolbert, M.A., Jimenez, J.L., Cordova, K.E., Ferrell, G.R. Secondary Organic Aerosol-Forming Reactions of Glyoxal with Amino Acids. *Environ. Sci. Technol.* **43**(8), 2818-2824 (2009).

15. Volkamer, R., Ziemann, P.J., Molina, M.J. Secondary Organic Aerosol Formation from Acetylene (C_2H_2): seed effect on SOA yields due to organic photochemistry in the aerosol aqueous phase. *Atmos. Chem. Phys.* **9**(6), 1907-1928 (2009).

16. Hopkins, R.J., Mitchem, L., Ward, A.D., Reid, J.P. Control and characterisation of a single aerosol droplet in a single-beam gradient-force optical trap. *Phys. Chem. Chem. Phys.* **6**(21), 4924-4927 (2004).

17. Galloway, M.M., Loza, C.L., Chhabra, P.S., Chan, A.W.H., Yee, L.D., Seinfeld, J.H., Keutsch, F.N. Analysis of photochemical and dark glyoxal uptake: Implications for SOA formation. *Geophys. Res. Lett.* **38**(17), L17811 (2011).

18. Loza, C.L., Chan, A.W.H., Galloway, M.M., Keutsch, F.N., Flagan, R.C., Seinfeld, J.H. Characterization of Vapor Wall Loss in Laboratory Chambers. *Environ. Sci. Technol.* **44**(13), 5074-5078 (2010).

19. Brandt, E.H. Levitation in Physics. *Science*. **243**(4889), 349-355 (1989).

20. Geng, D.L., Xie, W.J., Yan, N., Wei, B. Vertical vibration and shape oscillation of acoustically levitated water drops. *Appl. Phys. Lett.* **105**(10), 104101 (2014).

21. Santesson, S., Nilsson, S. Airborne chemistry: acoustic levitation in chemical analysis. *Anal. Bioanal. Chem.* **378**(7), 1704-1709 (2004).

22. Xie, W.J., Wei, B. Parametric study of single-axis acoustic levitation. *Appl. Phys. Lett.* **79**(6), 881-883 (2001).

23. Saha, A., Basu, S., Kumar, R. Velocity and rotation measurements in acoustically levitated droplets. *Phys. Lett. A*. **376**(45), 3185-3191 (2012).

24. Tian, Y., Holt, R.G., Apfel, R.E. A new method for measuring liquid surface tension with acoustic levitation. *Rev. Sci. Instrum.* **66**(5), 3349-3354 (1995).

25. Leiterer, J., Delissen, F., Emmerling, F., Thunemann, A.F., Panne, U. Structure analysis using acoustically levitated droplets. *Anal. Bioanal. Chem.* **391**(4), 1221-1228 (2008).

26. Grier, D.G. A revolution in optical manipulation. *Nature*. **424**(6950), 810-816 (2003).

27. Ashkin, A. Forces of a single-beam gradient laser trap on a dielectric sphere in the ray optics regime. *Biophys. J.* **61**(2), 569-582 (1992).

28. Neuman, K.C., Nagy, A. Single-molecule force spectroscopy: optical tweezers, magnetic tweezers and atomic force microscopy. *Nat. Methods*. **5**(6), 491-505 (2008).

29. Nieminen, T.A., Knöner, G., Heckenberg, N.R., Rubinsztein-Dunlop, H. Physics of Optical Tweezers. **82**, 207-236 (2007).

30. Neto, P.A.M., Nussenzveig, H.M. Theory of optical trapping. *Europhys. Lett.* **50**(5), 702-708 (2000).

31. Wang, M.D., Yin, H., Landick, R., Gelles, J., Block, S.M. Stretching DNA with Optical Tweezers. *Biophys. J.* **72**(3), 1335-1346 (1997).

32. Sacconi, L., Tolić-Nørrelykke, I.M., Stringari, C., Antolini, R., Pavone, F.S. Optical micromanipulations inside yeast cells. *Appl. Opt.* **44**(11), 2001-2007 (2005).

33. Neuman, K.C., Chadd, E.H., Liou, G.F., Bergman, K., Block, S.M. Characterization of Photodamage to Escherichia coli in Optical Traps. *Biophys. J.* **77**(5), 2856-2863 (1999).

34. Ashkin, A., Dziedzic, J.M., Yamane, T. Optical trapping and manipulation of single cells using infrared laser beams. *Nature*. **330**(6150), 769-771 (1987).

35. Knox, K.J., Burnham, D.R., McCann, L.I., Murphy, S.L., McGloin, D., Reid, J.P. Observation of bistability of trapping position in aerosol optical tweezers. *J. Opt. Soc. Am. B*. **27**(3), 582-591 (2010).

36. Reid, J.P. Particle levitation and laboratory scattering. *J. Quant. Spectrosc. RA.* **110**(14-16), 1293-1306 (2009).

37. Guillon, M., Stout, B. Optical trapping and binding in air: Imaging and spectroscopic analysis. *Phys. Rev. A*. **77**(2), 023806 (2008).

38. Mitchem, L., Buajarern, J., Hopkins, R.J., Ward, A.D., Gilham, R.J.J., Johnston, R.L., Reid, J.P. Spectroscopy of Growing and Evaporating Water Droplets: Exploring the Variation in Equilibrium Droplet Size with Relative Humidity. *J. Phys. Chem. A*. **110**(26), 8116-8125 (2006).

39. King, M.D., Thompson, K.C., Ward, A.D. Laser Tweezers Raman Study of Optically Trapped Aerosol Droplets of Seawater and Oleic Acid Reacting with Ozone: Implications for Cloud-Droplet Properties. *J. Am. Chem. Soc.* **126**(51), 16710-16711 (2004).

40. Dholakia, K., Lee, W.M. Optical Trapping Takes Shape: The Use of Structured Light Fields. **56**, 261-337 (2008).

41. Carruthers, A.E., Reid, J.P., Orr-Ewing, A.J. Longitudinal optical trapping and sizing of aerosol droplets. *Opt. Express*. **18**(13), 14238-14244 (2010).

42. Arlt, J., Garces-Chavez, V., Sibbett, W., Dholakia, K. Optical micromanipulation using a bessel light beam. *Opt. Commun.* **197**(4-6), 239-245 (2001).

43. Meresman, H., Wills, J.B., Summers, M., McGloin, D., Reid, J.P. Manipulation and characterisation of accumulation and coarse mode aerosol particles using a Bessel beam trap. *Phys. Chem. Chem. Phys.* **11**(47), 11333-11339 (2009).

44. Canagaratna, M.R., Jayne, J.T., Jimenez, J.L., Allan, J.D., Alfarra, M.R., Zhang, Q., Onasch, T.B., Drewnick, F., Coe, H., Middlebrook, A., Delia, A., Williams, L.R., Trimborn, A.M., Northway, M.J., DeCarlo, P.F., Kolb, C.E., Davidovits, P., Worsnop, D.R. Chemical and microphysical characterization of ambient aerosols with the aerodyne aerosol mass spectrometer. *Mass. Spectrom. Rev.* **26**(2), 185-222 (2007).

45. Suess, D.T., Prather, K.A. Mass spectrometry of aerosols. *Chem. Rev.* **99**(10), 3007-3035 (1999).

46. Westphall, M.S., Jorabchi, K., Smith, L.M. Mass spectrometry of acoustically levitated droplets. *Anal. Chem.* **80**(15), 5847-5853 (2008).

47. Hilger, R.T., Westphall, M.S., Smith, L.M. Controlling charge on levitating drops. *Anal. Chem.* **79**(15), 6027-6030 (2007).

48. Smith, S.P., Bhalotra, S.R., Brody, A.L., Brown, B.L., Boyda, E.K., Prentiss, M. Inexpensive optical tweezers for undergraduate laboratories. *Am. J. Phys.* **67**(1), 26-35 (1998).

49. Marston, P.L. Shape oscillation and static deformation of drops and bubbles driven by modulated radiation stresses-Theory. *J. Acoust. Soc. Am.* **67**(1), 15-26 (1980).

50. Lee, C.P., Anilkumar, A.V., Wang, T.G. Static shape of an acoustically levitated drop with wave-drop interaction. *Phys. Fluids*. **6**(11), 3554 (1994).

51. Di Leonardo, R., Ruocco, G., Leach, J., Padgett, M., Wright, A., Girkin, J., Burnham, D., McGloin, D. Parametric Resonance of Optically Trapped Aerosols. *Phys. Rev. Lett.* **99**(1), (2007).

52. Milne, G., Jeffries, G.D., Chiu, D.T. Tunable generation of Bessel beams with a fluidic axicon. *Appl. Phys. Lett.* **92**(26), 261101 (2008).

53. Frey, B.L., Lin, Y., Westphall, M.S., Smith, L.M. Controlling gas-phase reactions for efficient charge reduction electrospray mass spectrometry of intact proteins. *J. Am. Soc. Mass Spectrom.* **16**(11), 1876-87 (2005).

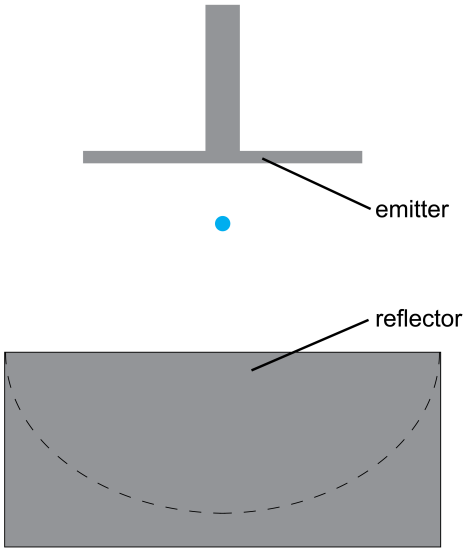

Figure 4.1 Schematic diagram of the acoustic levitator.

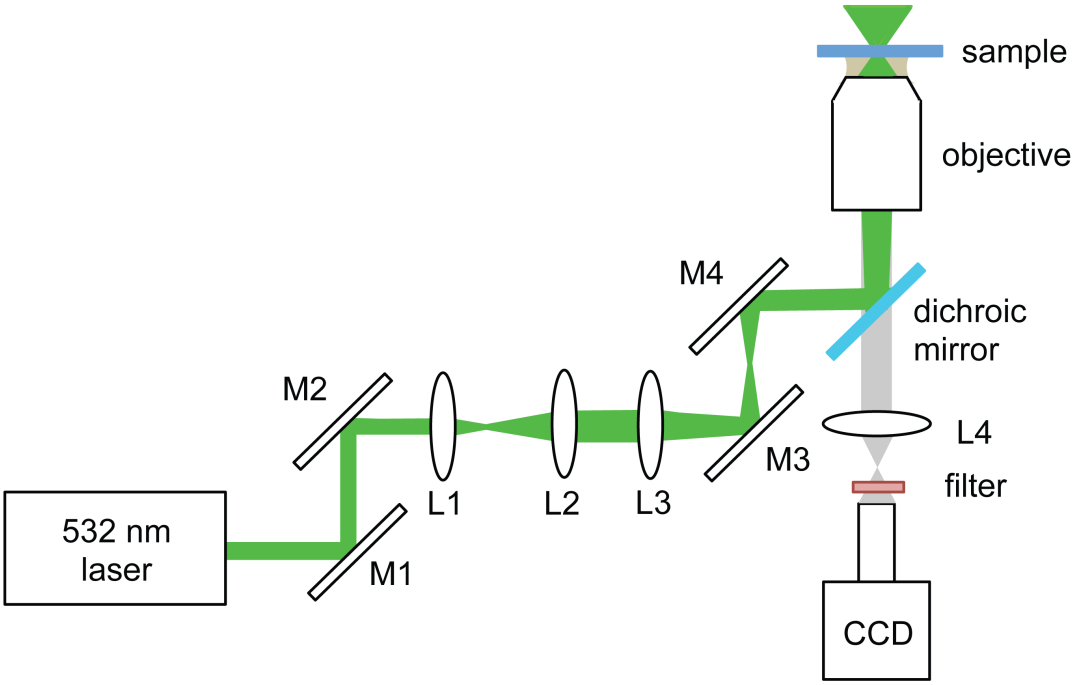

Figure 4.2 Schematic diagram of the Gaussiam beam optical tweezers. M: mirror. L: lens.

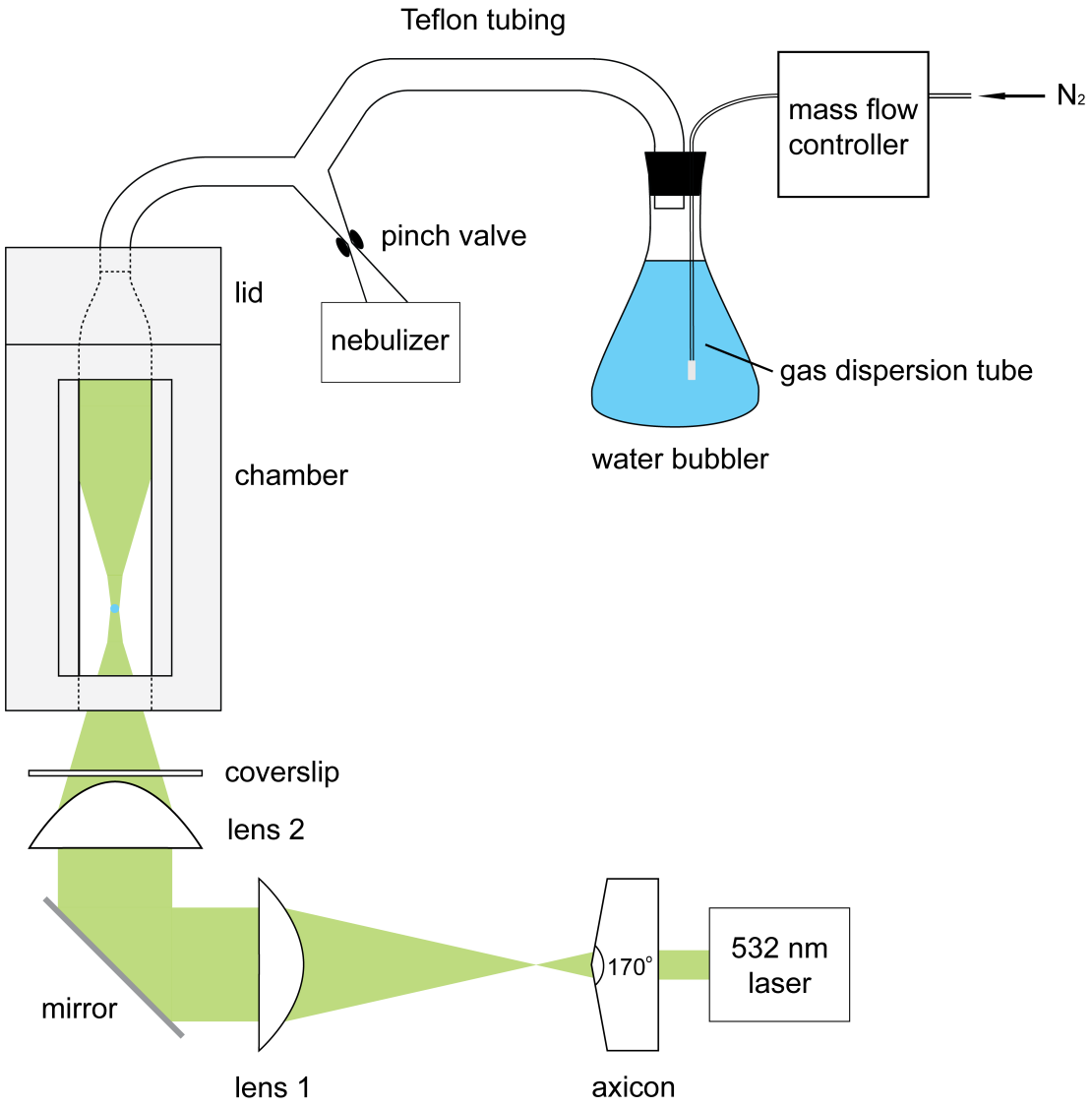

Figure 4.3 Schematic diagram of the Bessel beam optical tweezers.

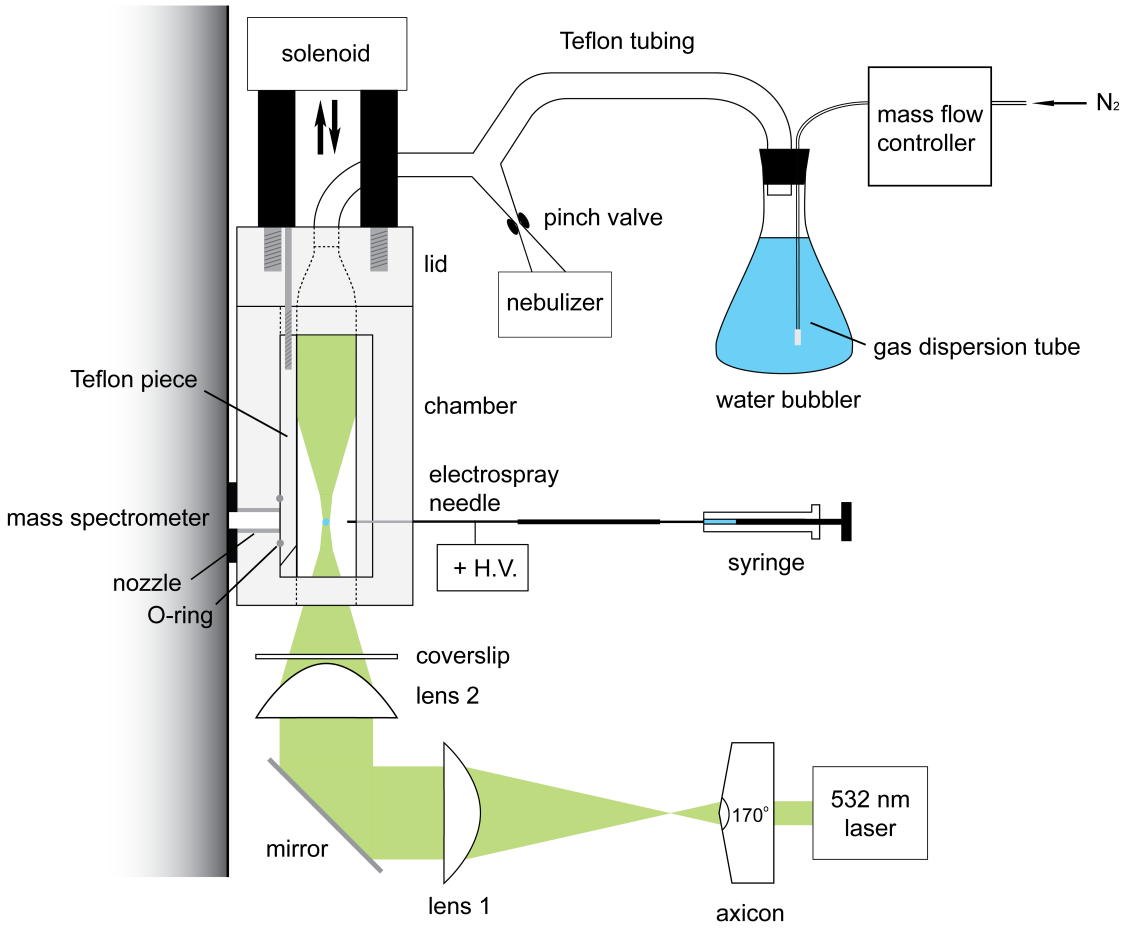

Figure 4.4 Schematic diagram of the bessel beam optical tweezers incorporated with the homemade ESI source and a mass spectrometer.

Figure 4.5 A droplet about 0.8 mm in diameter levitated in the acoustic levitator. The round object in the back is a homemade inlet extension of a mass spectrometer.

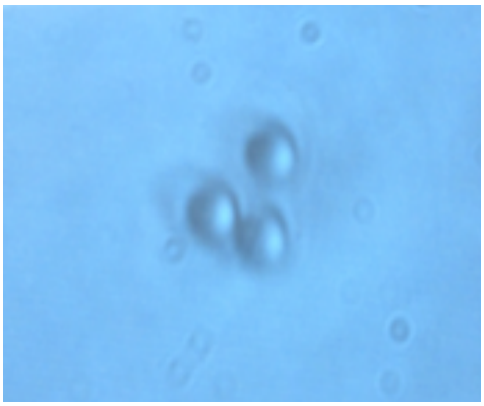

Figure 4.6 Three polystyrene beads trapped by the Gaussian beam optical tweezers observed on monitor.

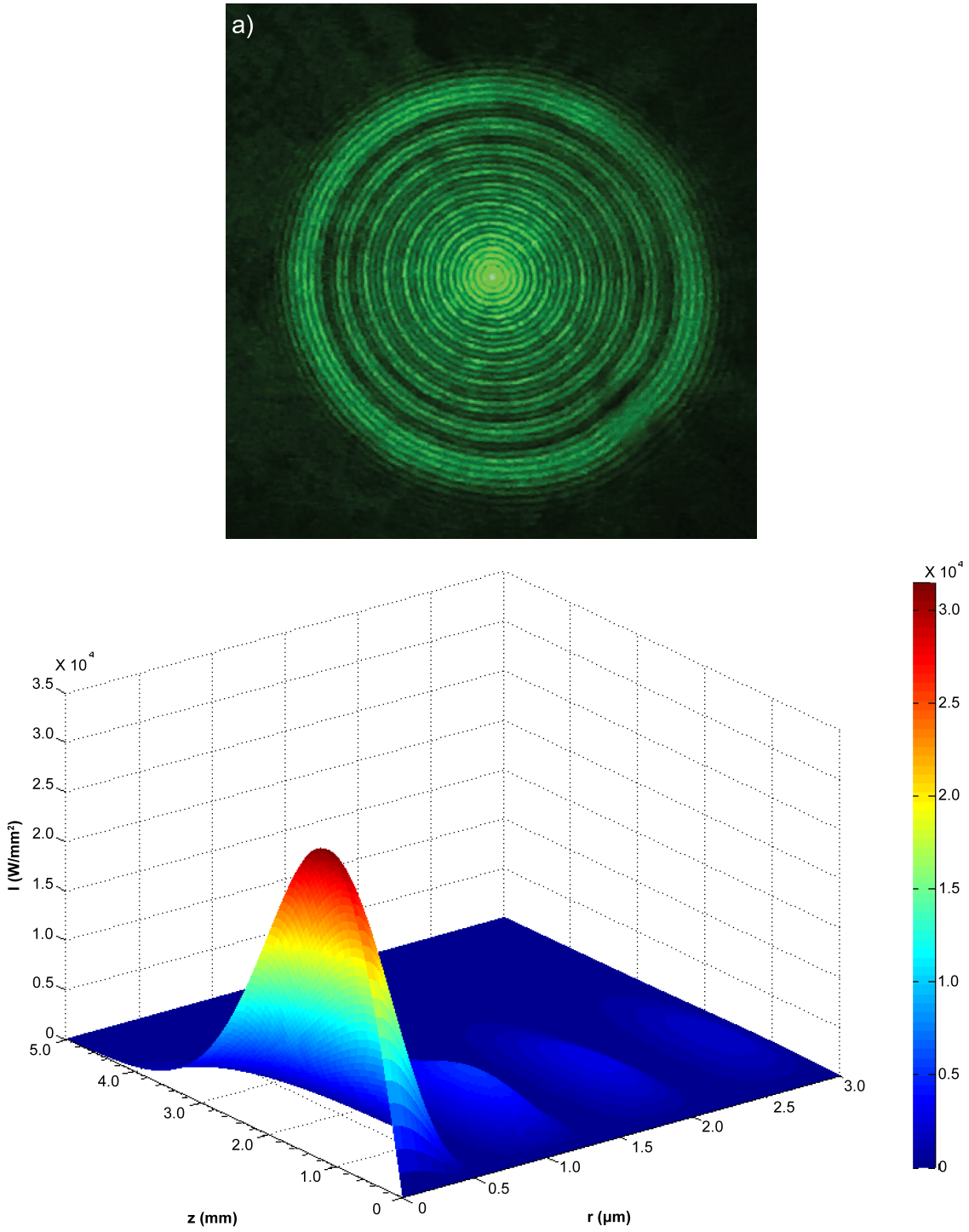

Figure 4.7 Cross-sectional profile a) and simulated intensity profile b) of the Bessel beam formed at the focus of lens 2.

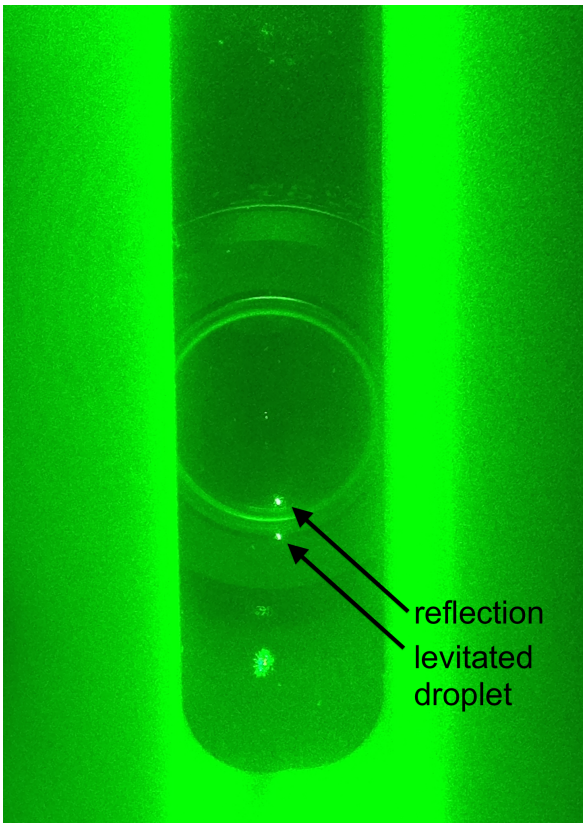

Figure 4.8 A levitated droplet in the Bessel beam optical tweezers observed through the glass window on the Teflon chamber. The bright dot above the levitated droplet is a reflection in the glass window. The round object in the back is the 10x objective.

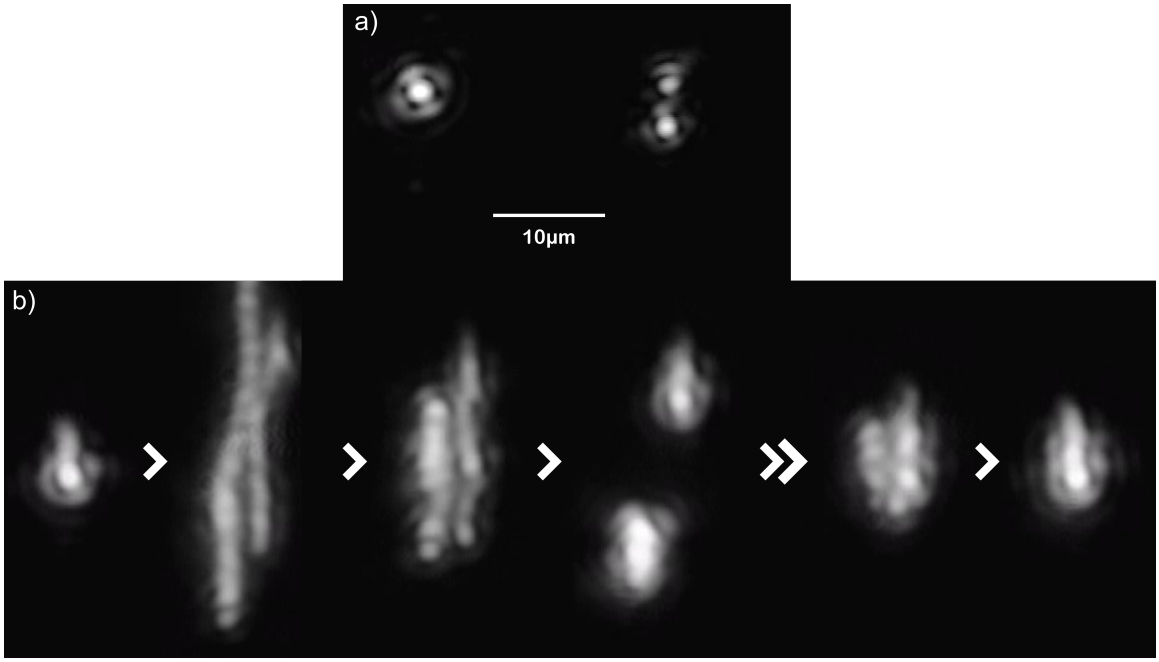

Figure 4.9 a) Two common patterns of the scattered light from the levitated droplet in the Bessel beam optical tweezers. b) Snapshots of the partition-and-reunion process of a levitated droplet.

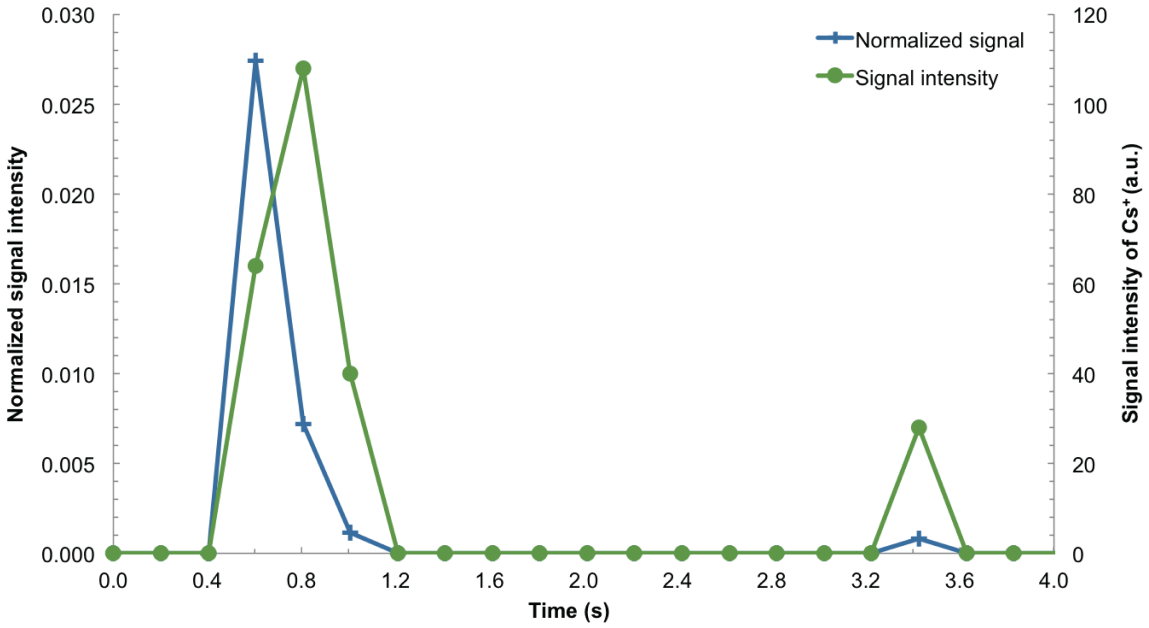

Figure 4.10 Extracted ion chromatogram of Cs^+ ions (m/z = 132.9) in a levitated droplet obtained by ESI-MS analysis. The signal intensity is normalized to that of a background ion (m/z = 217.1). The mass spectrometer acquisition frequency is 5 Hz.